

DYNAMICS OF MAGNETIZATION
INDUCED
BY ELECTRIC CURRENTS IN
TWO-DIMENSIONAL DIRAC
MATERIALS

© Robert Sokolewicz 2020

Dynamics of magnetization induced by electric currents in two dimensional dirac materials

PhD thesis, Radboud University

x + 358 pages; illustrated, with bibliographic references
and popular summary in English and Dutch

ISBN 978-94-028-1498-9

Printed in the Netherlands by Ipskamp Printing

DYNAMICS OF MAGNETIZATION
INDUCED
BY ELECTRIC CURRENTS IN TWO
DIMENSIONAL DIRAC
MATERIALS[9em]
PROEFSCHRIFT

ter verkrijging van de graad van doctor
aan de Radboud Universiteit Nijmegen
op gezag van de rector magnificus prof. dr. J.H.J.M. van Krieken,
volgens besluit van het college van decanen
in het openbaar te verdedigen op maandag 3 september 2020
om 14:30 uur precies

door

ROBERT JAN SOKOLEWICZ

geboren op 7 februari 1990
te Delft

PROMOTOR

Prof. dr. M.I. Katsnelson

CO-PROMOTOR

dr. M. Titov

MANUSCRIPTCOMMISSIE

Prof. dr. N.P. Landsman (voorzitter)

Prof. dr. J.S. Caux

(Universiteit van Amsterdam)

Dr. V. Cheianov (Universiteit Leiden)

Prof. dr. J. Schmalian (Karlsruher

Institut für Technologie, Duitsland)

Prof. dr. H. Waalkens

(Rijksuniversiteit Groningen)

Ohana means family.
Family means nobody gets left behind, or forgotten.
— Lilo & Stitch

Dedicated to the loving memory of Rudolf Miede.
1939–2005

CONTENTS

1	DIFFUSIVE SPIN-ORBIT TORQUES IN A TWO-DIMENSIONAL DIRAC FERROMAGNET	1
1.1	Kubo formula	13
1.2	Calculation of the spin-spin correlator	15
1.3	Limiting behavior of $m(t)$	18
2	SPIN-ORBIT TORQUES IN RASHBA HONEYCOMB ANTIFERROMAGNETS	27
2.1	Introduction	30
2.2	Model	31
2.3	Scattering approach	34
2.4	Spin-orbit torques	37
2.5	Microscopic LLG equation	38
2.6	Symmetry consideration	40
2.7	Results for symmetric model	42
2.7.1	General	42
2.7.2	Metal regime	43
2.7.3	Half-metal regime	44
2.8	Asymmetric coupling model	45
2.9	Conclusions	49
3	GILBERT DAMPING IN RASHBA HONEYCOMB ANTIFERROMAGNETS	51
3.1	Introduction	54
3.2	Phenomenology of AFM dynamics	57
3.3	Microscopic model	60
3.4	Conductivity	62
3.5	Spin-orbit torque	62
3.6	Gilbert damping	65
3.7	Qualitative consideration	66
3.8	Conclusions	68
3.9	Model system	68
3.10	Linear Response tensors	69
3.11	Vertex correction	72
3.12	Finite magnetization	73

DIFFUSIVE SPIN-ORBIT TORQUES IN A TWO-DIMENSIONAL DIRAC FERROMAGNET

We investigate spin-orbit torques on magnetization in an insulating ferromagnetic (FM) layer that is brought into a close proximity to a topological insulator (TI). In addition to the well-known field-like spin-orbit torque, we identify an anisotropic anti-damping-like spin-orbit torque that originates in a diffusive motion of conduction electrons. This diffusive torque is vanishing in the limit of zero momentum (i. e. for spatially homogeneous electric field or current), but may, nevertheless, have a strong impact on spin-torque resonance at finite frequency provided external field is neither parallel nor perpendicular to the TI surface. The required electric field configuration can be created by a grated top gate.

It is widely known that spin-orbit interaction provides an efficient way to couple electronic and magnetic degrees of freedom. It is, therefore, no wonder that the largest torque on magnetization, which is also referred to as the spin-orbit torque, emerges in magnetic systems with strong spin-orbit interaction [miron_current-driven_2010, haney_current_2013] as has been long anticipated [dyakonov_current-induced_1971].

The spin-orbit coupling may be enhanced by confinement potentials in effectively two-dimensional systems consisting of conducting and magnetic layers. The in-plane current may efficiently drive domain walls or switch magnetic orientation in such structures with the help of spin-orbit torque [awschalom2009trend, manchon_theory_2008, garate_influence_2009, manchon2009theory], which is present even for uniform magnetization, or with the help of spin-transfer torque, which requires the presence of magnetization gradient (due to e. g. domain wall) [slonczewski_current-driven_1996, berger_emission_1996, ralph_spin_2008, stiles_anatomy

Topological insulators (TI) [fu_topological_2007, moore_topological_2007, roy_topological, hsieh_topological_2008] may be thought as materials with an ultimate spin-orbit coupling. Indeed, the effective Hamiltonian of conduction electrons at the TI surface contains essentially nothing but spin-orbit interaction term that provides a perfect spin-momentum locking. Thus, the magnetization dynamics in a thin ferromagnetic (FM) film in a proximity to TI surface is expected to be strongly affected by electric currents and/or electric fields [qi_fractional_2008]. There seems to be, indeed, a substantial experimental evidence that the efficiency of domain switching in TI/FM heterostructures is dramatically enhanced as compared to that in metals [mellnik_spin-transfer_2014, wang_SOT_BiSe_2014, fan_magnetization_2014, Fan_SOT_TI_2016, Yasuda_SOT_BiSbTe_2017, Cha2018].

Nowadays the symmetry of spin-orbit torques is routinely inferred from the ferromagnetic resonance measurements in which an alternating microwave-frequency current (with frequencies 7 – 12 GHz) is applied within the sample plane [mellnik_spin-transfer_2014, Ralph2011SOTFMresonance, Wang2015_SOTHfCoFeB, Ralph2016SOTWTe2, Ralph2018SOT].

In this work we identify a novel anti-damping-like torque originating in a diffusive motion of conduction electrons at the TI surface. Such a torque originates in a non-local diffusive response of z component of the conduction electron spin density to the in-plane electric field. The non-locality of the response is determined by the so-called diffusion pole in analogy to the density-density response of a disordered system. It is, however, important that the diffusive response of the spin-density in the TI is always present in the perpendicular-to-the-plane component of the spin density, irrespective of the magnetization direction in the FM. In non-topological FM/metal systems such a diffusive response is present only in the spin density component that is directed along the local magnetization of the FM. Thus, the diffusive anti-damping spin-orbit

Figure 1.1: Proposed experimental setup. Non-homogeneous in-plane electric field components are created by an ac top-gate voltage V_{top} that induce a strong diffusive spin-orbit torque (1.4) of the damping-like symmetry. An effective magnetic field \mathbf{H} is directed at the angle χ with respect to \hat{z} .

Figure 1.2: Proposed experimental setup. Non-homogeneous in-plane electric field components are created by an ac top-gate voltage V_{top} that induce a strong diffusive spin-orbit torque (1.4) of the damping-like symmetry. An effective magnetic field \mathbf{H} is directed at the angle χ with respect to \hat{z} .

torque, that we describe below, is specific for the TI/FM interfaces. Similarly, we identify a strong anisotropy of the Gilbert damping in the TI/FM system due to a combination of electron elastic scattering on non-magnetic impurities and a spin-momentum locking in the TI.

Diffusive anti-damping spin-orbit torque, that we are going to study, can be related to a response of conduction electron spin density to electric field at a finite, but small, frequency and momentum. Such a field can be created e. g. by applying an *ac* gate voltage to a grated top-gate as shown in Fig. 1.2. The presence of the diffusive spin-orbit torque can be detected by rather unusual spin-orbit-torque resonances in the TI/FM structures that we also investigate in this work.

Microscopic theory of current-induced magnetization dynamics in TI/FM heterostructures has been so far limited to some particular cases: (i) specific direction of magnetization and (ii) the limit of vanishing exchange interaction between FM angular momenta and the spins of conduction electrons. In particular, an analytic estimate of spin-transfer and spin-orbit torques in TI/FM bilayer has been given in Ref. [sakai_spin_2014] for magnetization perpendicular to the TI surface. An attempt to generalize these results to arbitrary magnetization direction has been undertaken more recently in Ref. [ndiaye_dirac_2017]. The non-local transport on a surface of the TI has been first discussed in Ref. [burkov_spin_2010]. The results of this work has been later applied to TI/FM systems [taguchi_spin-charge_2015, shintani_spin_2016] in a perturbative approach with respect to a weak s-d-type exchange. The non-local behavior of non-equilibrium out-of-plane spin polarization in TI/FM systems, which gives rise to diffusive spin-orbit torques, have been, however, overlooked in all these publications.

To describe magnetization dynamics at a TI/FM interface we employ an effective two-dimensional Dirac model for conduction electrons

$$\mathcal{H} = v [(\mathbf{p} - e\mathbf{A}) \times \boldsymbol{\sigma}]_z - \Delta_{\text{sd}} \mathbf{m} \cdot \boldsymbol{\sigma} + V(\mathbf{r}), \quad (1.1)$$

where \mathbf{A} stands for the vector potential, $e = -|e|$ is the electron charge, z is the direction perpendicular to the TI surface, v is the effective velocity of Dirac electrons, and $V(\mathbf{r})$ is a disorder potential that models the main relaxation mechanism of conduction electrons. The energy $\Delta_{sd} = J_{sd}S$ is characterizing the local exchange interaction $\mathcal{H}_{ex} = -J_{sd} \sum_n \mathbf{S}_n \cdot \mathbf{c}_n^\dagger \boldsymbol{\sigma} \mathbf{c}_n$ between localized classical magnetic moments \mathbf{S}_n on FM lattice (with conserved absolute value $S = |\mathbf{S}_n|$ per unit cell area \mathcal{A}) and the electron spin density (represented by the vector operator $\boldsymbol{\sigma} = (\sigma_x, \sigma_y, \sigma_z)$ on the TI surface) [**sdmodel**]. Here σ_α stand for Pauli matrices and J_{sd} quantifies the s-d-type exchange interaction strength.

Classical equation of motion for the unit magnetization vector $\mathbf{m} = \mathbf{S}/S$ is determined by the s-d like exchange interaction \mathcal{H}_{ex} as

$$\partial \mathbf{m} / \partial t = \gamma \mathbf{H} \times \mathbf{m} + \mathbf{T}, \quad \mathbf{T} = (J_{sd}\mathcal{A}/\hbar) \mathbf{m} \times \mathbf{s}, \quad (1.2)$$

where $\hbar = h/2\pi$ is the Planck constant and γ is a gyromagnetic ratio for the FM spin. The effective field \mathbf{H} represents the combined contribution of external magnetic field and the field produced by neighboring magnetic moments in the FM (e. g. due to direct exchange), while the term \mathbf{T} represents the effect of the conduction electron spin density $\mathbf{s}(\mathbf{r}, t) = \langle \mathbf{c}_n^\dagger \boldsymbol{\sigma} \mathbf{c}_n \rangle$ on the TI surface.

To quantify the leading contributions to \mathbf{T} we microscopically compute: i) a linear response of \mathbf{s} to the in-plane electric field $\mathbf{E}(\mathbf{r}, t) = \mathbf{E}_{q,\omega} \exp(-i\omega t + i\mathbf{q} \cdot \mathbf{r})$; and ii) a linear response of \mathbf{s} to the time derivative $\partial \mathbf{m} / \partial t$. The former response defines the spin-orbit torque, while the latter one does the Gilbert damping.

Before we proceed with the analysis we shall note that the velocity operator $\mathbf{v} = v(\boldsymbol{\sigma} \times \hat{\mathbf{z}})$ in the model of Eq. (1.1) is directly related to the spin operator $\boldsymbol{\sigma}$. As the result, the response of the in-plane spin density $\mathbf{s}_{\parallel} = (s_x, s_y)$ to electric field $\mathbf{E} = -\partial \mathbf{A} / \partial t$ is defined by the conductivity tensor [**ndiaye_dirac_2017**, **Ghosh18**]. This also means that the non-equilibrium contribution to \mathbf{s}_{\parallel} from the electric current density \mathbf{J} is given by $\mathbf{s}_{\parallel} = (\hat{\mathbf{z}} \times \mathbf{J})/ev$ for any frequency and momentum irrespective of type of scattering for conduction electrons and even beyond the linear response.

Thus, the response of \mathbf{s}_{\parallel} defines an exceptionally universal field-like spin-orbit torque

$$\mathbf{T}_{FL}^{SOT} = (J_{sd}\mathcal{A}/\hbar ev) \mathbf{m} \times (\hat{\mathbf{z}} \times \mathbf{J}), \quad (1.3)$$

that acts in the same way as in-plane external magnetic field applied perpendicular to the charge current.

Apart from the universal response of \mathbf{s}_{\parallel} there might also exists a non-equilibrium spin polarization s_z perpendicular to the TI surface. This component plays no role in Eq. (1.2) for $\mathbf{m} = \pm \hat{\mathbf{z}}$ due to the vector product involved. Also, the s_z component is vanishing by symmetry for $\mathbf{m} = \mathbf{m}_{\parallel}$, where we decompose $\mathbf{m} = \mathbf{m}_{\parallel} + \mathbf{m}_{\perp}$ to in-plane and perpendicular-to-the plane components.

We find, however, that for a general direction of \mathbf{m} , the spin density s_z may be strongly affected by the in-plane electric field at a small but finite frequency and a small but finite wave vector. In the leading approximation the result can be cast in the following form

$$\mathbf{T}_{\text{diff}}^{\text{SOT}} = \eta \mathbf{m} \times \mathbf{m}_{\perp} \frac{iD \mathbf{q} \cdot \mathbf{E}}{i\omega - Dq^2}, \quad \eta = \frac{eJ_{\text{sd}}^2 \mathcal{A}S}{2\pi\hbar^3 v^2}, \quad (1.4)$$

where D is a diffusion coefficient for conduction electrons at the TI surface and $\mathbf{E} = \mathbf{E}_{\mathbf{q},\omega} \exp(-i\omega t + i\mathbf{q} \cdot \mathbf{r})$. Note that the diffusive torque is non-linear with respect to \mathbf{m} and, from the point of view of the time reversal symmetry, is analogous to anti-damping torque. The denominator $i\omega - Dq^2$ in Eq. (1.4) reflects diffusive (Brownian) motion of conduction electrons that defines the time-delayed diffusive torque on magnetization $\mathbf{T}_{\text{diff}}^{\text{SOT}}$.

It is interesting to note that the torque of Eq. (1.4) has an anti-damping symmetry (when expressed through electric current rather than electric field). Moreover, the torque formally diverges as $1/q$ in the dc limit $\omega = 0$. This singularity is well-known in the theory of disordered systems [maleev1975corrections, m*aleev1976corrections, althshuler1985electron] and originates in the diffusive (Brownian) motion of conduction electrons in a disorder potential. The dc limit singularity in Eq. (1.4) is, in fact, regularized by the dephasing length of conduction electrons on the surface of the TI. The length is strongly temperature and material dependent and, at low temperatures, can reach hundreds of microns. Thus, the result of Eq. (1.4) also predicts large anti-damping spin-orbit torque in the dc-limit that originates in a mechanism which is specific for the TI interface.

In order to derive the result of Eq. (1.4) and the expressions for Gilbert damping we shall adopt a particular relaxation model for both spin and orbital angular momenta of conduction electrons. For the model of Eq. (1.1) those are provided by scattering on disorder potential. We choose the latter to be the white-noise Gaussian disorder potential that is fully characterized by a single dimensionless parameter $\alpha \ll 1$,

$$\langle V(\mathbf{r}) \rangle = 0, \quad \langle V(\mathbf{r})V(\mathbf{r}') \rangle = 2\pi\alpha (\hbar v)^2 \delta(\mathbf{r} - \mathbf{r}'), \quad (1.5)$$

where angular brackets stay for the averaging over the ensemble of disordered systems.

Since both the vector potential \mathbf{A} and the magnetization \mathbf{m} couple to spin operators in Eq. (1.1), the linear response of s to $\mathbf{E} = -\partial\mathbf{A}/\partial t$ and $\partial\mathbf{m}/\partial t$ is defined in the frequency-momentum domain as

$$s = (v^2\hbar)^{-1} \hat{\mathbf{K}}(\mathbf{q}, \omega) [\text{ev}(\mathbf{E} \times \hat{\mathbf{z}}) - i\omega\Delta_{\text{sd}} \mathbf{m}]. \quad (1.6)$$

Here, the dimensionless 9-component tensor $\hat{K}(\mathbf{q}, \omega)$ is given by the Kubo formula

$$\hat{K}_{\alpha\beta}(\mathbf{q}, \omega) = v^2 \int \frac{d^2\mathbf{p}}{(2\pi)^2} \text{Tr} \left\langle \sigma_\alpha G_{\mathbf{p}+\hbar\mathbf{q}, \varepsilon+\hbar\omega}^R \sigma_\beta G_{\mathbf{p}, \varepsilon}^A \right\rangle, \quad (1.7)$$

where the notation $G_{\mathbf{p}, \varepsilon}^{R(A)}$ stands for the retarded (advanced) Green's function for the Hamiltonian of Eq. (1.1), the angular brackets denote the averaging over disorder realizations, while the energy ε refers to the Fermi energy (zero temperature limit is assumed).

The tensor \hat{K} can be represented by the matrix

$$\hat{K} = \begin{pmatrix} \sigma_{xx} & \sigma_{xy} & Q_y \\ \sigma_{yx} & \sigma_{yy} & -Q_x \\ Q_y & -Q_x & \zeta \end{pmatrix}, \quad (1.8)$$

of which $\sigma_{\alpha\beta}$ are the components of the two dimensional conductivity tensor at the TI surface (all conductivities are expressed in the units of e^2/h), the vector \mathbf{Q} defines the diffusive spin-orbit torque of Eq. (1.4) (its contribution to Gilbert damping is negligible), while ζ determines the response of s_z to $\partial m_z / \partial t$. The components of \hat{K} correspond to different responses at different limits. When discussing the response to an electric field $\mathbf{E}_{q\omega}$ we are primarily interested in the limit $\omega \ll Dq^2$, whereas the response to time-derivative of magnetization \mathbf{m} is defined by the limit $q \rightarrow 0$.

In the linear response theory of Eq. (1.6) one needs to compute the tensor in Eq. (3.24) for a constant direction \mathbf{m} and for $\mathbf{A} = 0$. In usual systems (conducting ferromagnets) the response of s in the direction of \mathbf{m} is always diffusive. This response, however, plays no role in the torque since $\mathbf{T} \propto \mathbf{m} \times \mathbf{s}$. The situation at the TI surface is, however, special. Here, the in-plane components of magnetization m_x, m_y play no role in Eq. (1.1), since those are simply equivalent to a constant in-plane vector potential for conduction electrons and, therefore, can be excluded by a gauge transform (shift of the Dirac cone). Consequently, all observable quantities in the model (including all components of the tensor \hat{K}) may only depend on the field $\Delta_z = \Delta_{sd} m_z$. As the result, the diffusive response occurs exclusively in s_z component of spin polarization and can easily enter the expression for the torque.

The conductivity tensor in the model of Eqs. (1.1, 1.5) has been analyzed in detail in Ref. [ivanEPL] in the limit $\omega = q = 0$ (and for $\alpha \ll 1$) with the result $\sigma_{xx} = \sigma_{yy} = \sigma_0$ and $\sigma_{xy} = -\sigma_{yx} = \sigma_H$, where

$$\sigma_0 = \frac{\varepsilon^2 - \Delta_z^2}{\pi\alpha(\varepsilon^2 + 3\Delta_z^2)}, \quad \sigma_H = \frac{8\varepsilon\Delta_z^3}{(\varepsilon^2 + 3\Delta_z^2)^2}. \quad (1.9)$$

Since the anomalous Hall conductivity $\sigma_H \propto \alpha \sigma_0$ is sub-leading with respect to σ_0 , it has to be computed beyond the Born approximation (see Refs. [ivanEPL, ivanPRL, ivanPRB]).

Here we generalize the analysis to calculate the tensor \hat{K} for finite ω and q assuming $\alpha \ll 1$, $\omega \tau_{tr} \ll 1$, and $\omega \propto Dq^2$, where $D = \hbar v^2 \sigma_0 / \varepsilon$ is the diffusion coefficient and $\tau_{tr} = \hbar \varepsilon \sigma_0 / (\varepsilon^2 + \Delta_z^2)$ is the transport scattering time for the problem. In real samples $\tau_{tr} = 0.01 - 1$ ps [kong_rapid_2011, kamboj_probing_2017, huang_enhancement_2017, xiang_transport_2014].

The main building block of our analysis is the averaged Green's function in the first Born approximation

$$G_{\mathbf{p},\varepsilon}^R = \frac{\varepsilon^R + v(\mathbf{p} \times \boldsymbol{\sigma})_z - \Delta_z^R \sigma_z}{(\varepsilon^R)^2 - v^2 p^2 - (\Delta_z^R)^2}, \quad (1.10)$$

where the complex parameters $\varepsilon^R = \varepsilon(1 + i\pi\alpha/2)$ and $\Delta_z^R = \Delta_z(1 - i\pi\alpha/2)$ are found from the corresponding self-energy

$$\Sigma^R(\varepsilon) = 2\pi\alpha v^2 \int \frac{d^2 \mathbf{p}}{(2\pi)^2} G_{\mathbf{p},\varepsilon'}^R, \quad (1.11)$$

that gives rise to $\text{Im} \Sigma^R = -\pi\alpha(\varepsilon - \Delta_z \sigma_z)/2$ (strictly speaking, the RG analysis [ivanEPL] has to be applied). In the Green's function of Eq. (1.10) we shift the momentum \mathbf{p} such that there is no direct dependence on the in-plane magnetization components m_x and m_y .

The next step in disorder-averaging requires the computation of vertex corrections. This means we need to replace the spin operator σ_α with a vertex corrected spin operator $\sigma_\alpha^{\text{vc}}$ in the ladder approximation as depicted in Fig. 3.4(e). The crossed diagrams in Fig. 3.4(b-d) give a contribution to the components of \hat{K} of the order $\mathcal{O}(\alpha^0)$. The only components that are modified to this order are those corresponding to the Hall conductivity (i.e. σ_{xy} and σ_{yx}). Details of this calculation can be found Ref. [ivanEPL].

The dressing of σ_α with a single disorder line is denoted by $\sigma_\alpha^{1 \times \text{dr}}$ and is conveniently represented in the matrix form by introducing a matrix \hat{M} with 16 components $M_{\alpha\beta}$ for $\alpha, \beta = 0, x, y, z$ (with $\sigma_0 = 1$)

$$\sigma_\alpha^{1 \times \text{dr}} = 2\pi\alpha v^2 \int \frac{d^2 \mathbf{p}}{(2\pi)^2} G_{\varepsilon+\omega, \mathbf{p}+\mathbf{q}}^A \sigma_\alpha G_{\mathbf{p}}^R = \pi\alpha M_{\alpha\beta} \sigma_\beta, \quad (1.12)$$

where the summation of the repeating index $\beta = 0, x, y, z$ is assumed. Full expressions of the components of \hat{M} up to second order in ω and q are given by Eq. (1.30a-f).

In our calculation the terms of the order of $\alpha \ln p_{\text{cutoff}}/\varepsilon$ (where p_{cutoff} is the ultraviolet momentum cut-off) is disregarded with respect to 1. This approxima-

Figure 1.3: Diagrams considered in the calculation of \hat{K} : (a) non-crossing diagram, (b) X diagram, (c-d) Ψ diagrams. Green areas indicate the ladder summation (e) for the vertex correction in the non-crossing approximation [ivanEPL].

tion is legitimate since we assume that all model parameters ϵ , Δ_{sd} and α are first renormalized such that $p_{\text{cutoff}} \approx \epsilon$.

It is, then, easy to see that the vertex-corrected spin operator is readily obtained from the geometric series of powers of $\pi\alpha\hat{M}$,

$$\begin{aligned}\sigma_{\alpha}^{\text{vc}} &= \sigma_{\alpha} + \pi\alpha\hat{M}_{\alpha\beta}\sigma_{\beta} + (\pi\alpha)^2(\hat{M}^2)_{\alpha\beta}\sigma_{\beta} + \dots \\ &= [1 - \pi\alpha\hat{M}]_{\alpha\beta}^{-1}\sigma_{\beta}.\end{aligned}\quad (1.13)$$

Thus, in the non-crossing approximation (illustrated in Fig. 3.4 (a)), one simply finds $\hat{K} = \hat{M}[1 - \pi\alpha\hat{M}]^{-1}$.

Dressed spin-spin correlators are defined by the components $\hat{K}_{\alpha\beta}$ with $\alpha, \beta = x, y, z$. The vector \mathbf{q} selects a particular direction in space, that makes the conductivity tensor anisotropic. By choosing x direction along the \mathbf{q} vector, we find the conductivity components $\sigma_{xx} = \sigma_0$, $\sigma_{xy} = -\sigma_{yx} = \sigma_H$, and $\sigma_{yy} = i\omega\sigma_0/(i\omega - Dq^2)$, where we have kept only the leading terms in the limits $\alpha \ll 1$, $\omega\tau_{\text{tr}} \ll 1$ (more general expressions are given by Eqs. (1.32a-d)). We can see that σ_{yy} component also acquires a diffusion pole. One needs to go beyond the non-crossing approximation in the computation of anomalous Hall conductivity [ivanEPL, ivanPRL, ivanPRB].

Clearly, the components $\sigma_{\alpha\beta}$ define the field-like contribution $T_{\text{FL}}^{\text{SOT}}$ that has been already discussed above. It is interesting to note that the conductivity is isotropic $\sigma_{xx} = \sigma_{yy} = \sigma_0$ only if the limit $q = 0$ is taken before the limit $\omega = 0$. If the limit $\omega = 0$ is taken first, the conductivity remains anisotropic with respect to the direction of \mathbf{q} even for $q = 0$.

The vector $\mathbf{Q} = (Q_x, Q_y)$ quantifies both the response of s_z to electric field or to $\partial\mathbf{m}_{\parallel}/\partial t$ as well as the response of s_{\parallel} to $\partial\mathbf{m}_z/\partial t$. From Eq. (3.24) we find,

$$\mathbf{Q}(\omega, \mathbf{q}) = \frac{\Delta_z}{\hbar v} \frac{iD\mathbf{q}}{i\omega - Dq^2} (1 + \mathcal{O}(\omega\tau_{\text{tr}})), \quad (1.14)$$

where we again assumed $\omega\tau_{\text{tr}} \ll 1$. The result of Eq. (1.14), then, corresponds to an additional diffusive spin-orbit torque of the form Eq. (1.4).

Finally, the response of s_z to $\partial\mathbf{m}_z/\partial t$ is defined by

$$\zeta = \frac{\Delta_z^2}{i\hbar\epsilon\omega} \left(1 + \mathcal{O}(\omega^2\tau_{\text{tr}}^2)\right), \quad (1.15)$$

where the limit $q = 0$ is taken. Thus, we find from Eq. (1.6) that there exists no response of s_z to $\partial\mathbf{m}_z/\partial t$. Instead, the quantity ζ defines the additional

spin polarization in z -direction $\delta s_z = -\Delta_{\text{sd}}^3 m_z^3 / (2\pi\hbar^2 v^2 \varepsilon)$ that we ignore below. Eqs. (1.14,1.15) including subleading terms in $\omega\tau_{\text{tr}}$ are presented in Eq. (1.33).

We also note, that $Q(q=0)=0$, hence there is no term in s_z that is proportional to $\partial \mathbf{m} / \partial t$. This reflects highly anisotropic nature of the Gilbert damping in the model of Eq. (1.1).

The remaining parts of the Gilbert damping can be cast in the following form

$$\mathbf{T}^{\text{GD}} = \frac{J_{\text{sd}}^2 AS}{\pi\hbar^2 v^2} \mathbf{m} \times \left(\sigma_0 \frac{\partial \mathbf{m}_{\parallel}}{\partial t} + \frac{\sigma_H}{m_z} \frac{\partial \mathbf{m}_{\parallel}}{\partial t} \times \mathbf{m}_{\perp} \right), \quad (1.16)$$

where the coefficients, σ_0 and σ_H/m_z from Eq. (1.9) depend on m_z^2 , which is yet another source of the Gilbert damping anisotropy. We note, that even though Eq. (1.16) does not contain a term proportional to $\partial m_z / \partial t$, the existing in-plane Gilbert damping is sufficient to relax the magnetization along \hat{z} direction.

Despite strongly anisotropic nature of the diffusive torque (the torque is vanishing for purely in-plane or purely perpendicular to the plane magnetization), its strength for a generic direction of magnetization may be quite large. For example, for \mathbf{m} directed approximately at 45 degrees to the TI surface the ratio of amplitudes of diffusive and field like torques is readily estimated as

$$\frac{T_{\text{diff}}^{\text{SOT}}}{T_{\text{FL}}^{\text{SOT}}} = \frac{\Delta_{\text{sd}}}{\hbar q v} \frac{1}{\sigma_0}, \quad (1.17)$$

where we used the condition $\omega \ll Dq^2$. Let us assume that a top-gate in Fig. 1.2 induces an ac in-plane electric field with the characteristic period $2\pi q^{-1} \approx 1 \mu\text{m}$ and a typical FM resonance frequency, $\omega \approx 7\text{-}12 \text{ GHz}$. Then, for realistic materials one can estimate $Dq^2 \approx 100 \text{ GHz}$, hence $\omega \ll Dq^2$ indeed. For a typical velocity $v = 10^6 \text{ m/s}$ one finds $\hbar q v \approx 4 \text{ meV}$. Thus, the ratio $\Delta_{\text{sd}}/\hbar q v$ in Eq. (1.17) may reach three orders of magnitude, while the value of σ_0 is typically 10. This estimate suggests that, for a generic direction of \mathbf{m} , the magnitude of diffusive torque can become three orders of magnitude larger than that of the field-like spin-orbit torque.

The diffusive torque at the TI surface can be most directly probed by the corresponding spin-torque resonance. In this case, one can disregard the effect of the field like torque, so that Eq. (1.2) is simplified to

$$\frac{\partial \mathbf{m}}{\partial t} = \gamma \mathbf{H} \times \mathbf{m} + f(\mathbf{r}, t) \mathbf{m} \times \mathbf{m}_{\perp} + \alpha_G \mathbf{m} \times \frac{\partial \mathbf{m}_{\parallel}}{\partial t}, \quad (1.18)$$

where $\alpha_G = J_{\text{sd}}^2 AS \sigma_0 / (\pi(\hbar v)^2)$ is the Gilbert damping amplitude (which is a constant for $\varepsilon \gg \Delta_{\text{sd}}$), while the terms containing σ_H are omitted. The function

$$f(\mathbf{r}, t) = \eta \int d^2 \mathbf{r}' \int_{-\infty}^t dt' \frac{e^{-(\mathbf{r}-\mathbf{r}')^2/4D(t-t')}}{4\pi(t-t')} \nabla \cdot \mathbf{E}(\mathbf{r}', t'),$$

Figure 1.4: The projection $m_H(t)$ as simulated from Eq. (1.18) for $f_0 = 0.1 \omega_0$. Top panel illustrates the behavior at different frequencies for $\alpha_G = 0.005$. Lower panel illustrates the resonant behavior at different values of α_G . Dashed horizontal line corresponds to $m_H = 1/\sqrt{2}$. Dots indicate the asymptotic solution for $\alpha_G = 0$ as given by Eq. (1.19).

defines the strength of the diffusive spin-orbit torque (1.4) in real space and time.

Resonant magnetization dynamics defined by Eq. (1.18) is illustrated in Fig. 1.4 for \mathbf{H} directed at the angle $\chi = \pi/4$ with respect to \hat{z} and for frequencies that are close to the resonant frequency $\omega_0 = \gamma H$. The time evolution of magnetization projection $m_H = \mathbf{m} \cdot \mathbf{H}/H$ is induced by the diffusive torque with $f(t) = f_0 \cos \omega t$ (magnetization at different \mathbf{r} is simply different by a phase).

Resonant dynamics at $\omega = \omega_0$ in Eq. (1.18) consists of precession of \mathbf{m} around the vector \mathbf{H} such that the azimuth (precession) angle is changing linearly with time $\phi(t) = \omega_0 t - \pi/2$ (for $f_0 \ll \omega_0$ and $\alpha_G \ll 1$). In addition, the projection m_H oscillates between 1 and 0 on much larger time scales. Such oscillations are damped by a finite α_G to the limiting value $m_H = 1/\sqrt{2}$.

In the limit of vanishing Gilbert damping, $\alpha_G = 0$, one simply finds the result

$$m_H(t) = [\cosh(\frac{1}{4} f_0 t \sin(2\chi))]^{-1}, \quad (1.19)$$

which clearly illustrates the absence of the effect for both perpendicular-to-the-plane ($\chi = 0$) and in-plane ($\chi = \pi/2$) magnetization. The qualitative behavior at the resonance ($\omega = \omega_0$) is illustrated at the lower panel of Fig. 1.4 for different values of α_G .

In conclusion, we consider magnetization dynamics in a model TI/FM system at a finite frequency ω and \mathbf{q} vector. We identify novel diffusive anti-damping spin-orbit torque that is specific to TI/FM system. Such a torque is absent in usual (non-topological) FM/metal systems, where the diffusive response of conduction electron spin density is always aligned with the magnetization direction of the FM. In contrast, the electrons at the TI surface gives rise to singular diffusive response of the conduction electron spin-density in the direction perpendicular to the TI surface, irrespective of the FM magnetization direction. Such a response leads to strong non-adiabatic anti-damping spin-orbit torque that has a diffusive nature. This response is specific for a system with an ultimate spin-momentum locking and gives rise to abnormal anti-damping diffusive torque that can be detected by performing spin-torque resonance measurements. We also show that, in realistic conditions, the anti-damping like diffusive torque may become orders of magnitude larger than the usual field like spin-orbit torque. We investigate the peculiar magnetizations dynamics induced by the diffusive torque at the frequency of the ferromagnet resonance. Our theory also predicts ultimate anisotropy of the Gilbert damping in the TI/FM system. In

contrast, to the phenomenological approaches [vanderBijl2012, Hals2013] our microscopic theory is formulated in terms of very few effective parameters. Our results are complementary to previous phenomenological studies of Dirac ferromagnets [tserkovnyak_theory_2009, mahfouzi_spin-orbit_2012, katsnelson15, fischer_spin-torque_2016, yokoyama_theoretical_2010, yokoyama_current-induced_2011, siu_spin_2016, mahfouzi_antidamping_2016, soleimani_spin-orbit_2017, kurebayashi_microscopic_current-induced_2017, rodriguez-vega_giant_2016, qi_topological_2008, garate_inverse_2010, yokoyama_theoretical_2010, yokoyama_current-induced_2011, nomura_electric_2010, tserkovnyak_thin-film_2012-1, linder_improved_2014, tserkovnyak_spin_2015, ueda_topological_2012, liu_reading_2013, chang_nonequilibrium_2015, fischer_spin-torque_2016, mahfouzi_antidamping_2016, fujimoto_transport_2014, okuma_unconventional_2016].

1.1 KUBO FORMULA

The linear response formula used in the main text can be obtained in a Keldysh-framework. We start by introducing the Green function \mathcal{G} in rotated Keldysh space [see e.g. Ref. [rammer_quantum_1986]]

$$\mathcal{G} = \begin{pmatrix} G^R & G^K \\ 0 & G^A \end{pmatrix} \quad (1.20)$$

where R, A and K denote retarded, advanced and Keldysh Green functions respectively. In this notation a perturbation to a classical field $V(x, t)$ is given by

$$\delta\mathcal{G}(x_1, t_1; x_2, t_2) = \int dx_3 \int dt_3 \mathcal{G}^{(0)}(x_1, t_1; x_3, t_3) \hat{V}(x_3, t_3) \mathcal{G}^{(0)}(x_3, t_3; x_2, t_2) + \mathcal{O}(V^2) \quad (1.21)$$

with $\mathcal{G}^{(0)}$ equilibrium Green functions. The Wigner-transform of a function $F(x_1, t_1; x_2, t_2)$ is given by

$$F(x_1, t_1; x_2, t_2) = \int \frac{d^2p}{(2\pi\hbar)^2} \int \frac{d\varepsilon}{2\pi\hbar} e^{-i\varepsilon(t_1-t_2)/\hbar} e^{ip \cdot (x_1-x_2)/\hbar} F(\varepsilon, p, T) \quad (1.22)$$

with energy ε , momentum p , time $T = \frac{t_1+t_2}{2}$ and position $R = \frac{x_1+x_2}{2}$. In equilibrium the Green functions $\mathcal{G}^{(0)}$ do not depend on R and T , so that the momentum-frequency representation of Eq. (1.21) becomes $\delta\mathcal{G}(\varepsilon, \omega, p, q) = \mathcal{G}_{\varepsilon+, p+}^{(0)} V_{\omega, q} \mathcal{G}_{\varepsilon-, q-}^{(0)}$, with subscripts $\varepsilon_{\pm} = \varepsilon \pm \hbar\omega/2$ and $p_{\pm} = p \pm \hbar q/2$ and $V_{\omega, q}$ the Fourier transform of $V(R, T)$.

The spin density $s_{\omega,q}$ is given by

$$s_{\omega,q} = i\hbar \int \frac{d\varepsilon}{2\pi\hbar} \int \frac{d^2p}{(2\pi\hbar)^2} \text{Tr} [\delta G^<(\varepsilon, \omega, p, q, T) \sigma], \quad (1.23)$$

where,

$$\begin{aligned} \delta G^<(\varepsilon, \omega, p, q) = 1/2(\delta G^K(\varepsilon, \omega, p, q) \\ - \delta G^R(\varepsilon, \omega, p, q) + \delta G^A(\varepsilon, \omega, p, q)). \end{aligned} \quad (1.24)$$

In equilibrium we have the fluctuation-dissipation theorem $G_{\varepsilon_{\pm}, p_{\pm}}^K = (1 - 2f_{\varepsilon_{\pm}})(G_{\varepsilon_{\pm}, p_{\pm}}^R - G_{\varepsilon_{\pm}, p_{\pm}}^A)$ with $f_{\varepsilon_{\pm}}$ the Fermi distribution, so that the spin density now becomes

$$\begin{aligned} s_{\omega,q} = i\hbar \int \frac{d\varepsilon}{2\pi\hbar} \int \frac{d^2p}{(2\pi\hbar)^2} \text{Tr} \langle \\ - (f_{\varepsilon_+} - f_{\varepsilon_-}) \sigma G_{\varepsilon_+, p_+}^R V_{\omega,q} G_{\varepsilon_-, p_-}^A \\ - f_{\varepsilon_+} \sigma G_{\varepsilon_+, p_+}^R V_{\omega,q} G_{\varepsilon_-, p_-}^R \\ + f_{\varepsilon_-} \sigma G_{\varepsilon_+, p_+}^A V_{\omega,q} G_{\varepsilon_-, p_-}^A \rangle, \end{aligned} \quad (1.25)$$

where the angular brackets stands for impurity averaging. The latter amounts to the replacement of the Green's functions with the corresponding impurity averaged Greens functions (in Born approximation) and to the replacement of one of the spin operators with the corresponding vertex corrected operator (in the non-crossing approximation). The corrections beyond the non-crossing approximation are important for those tensor components that lack leading-order contribution [**ivanEPL**]. To keep our notations more compact we ignore here the fact that the Green's functions before disorder averaging lack translational invariance, i. e. depend on both Wigner coordinates: momentum and coordinate.

In the limit of small frequency, i.e. $\hbar\omega \ll \varepsilon$, we obtain $s_{\alpha} = s_{\alpha}^I + s_{\alpha}^{\text{II}}$,

$$\begin{aligned} s_{\alpha}^I = \frac{i\omega}{2\hbar} \int \frac{d\varepsilon}{2\pi} \int \frac{d^2p}{(2\pi)^2} \left(-\frac{\partial f}{\partial \varepsilon} \right) \times \\ \text{Tr} \langle 2\sigma_{\alpha} G_{\varepsilon_+, p_+}^R V_{\omega,q} G_{\varepsilon_-, p_-}^A - \sigma_{\alpha} G_{\varepsilon_+, p_+}^A V_{\omega,q} G_{\varepsilon_-, p_-}^A \\ - \sigma_{\alpha} G_{\varepsilon_+, p_+}^R V_{\omega,q} G_{\varepsilon_-, p_-}^R \rangle, \end{aligned} \quad (1.26)$$

$$\begin{aligned} s_{\alpha}^{\text{II}} = \frac{i}{\hbar} \int \frac{d\varepsilon}{2\pi} \int \frac{d^2p}{(2\pi)^2} f_{\varepsilon} \times \\ \text{Tr} \langle \sigma_{\alpha} G_{\varepsilon_+, p_+}^A V_{\omega,q} G_{\varepsilon_-, p_-}^A - \sigma_{\alpha} G_{\varepsilon_+, p_+}^R V_{\omega,q} G_{\varepsilon_-, p_-}^R \rangle, \end{aligned} \quad (1.27)$$

where s^I and s^{II} are the Kubo and Streda contributions respectively. The Streda contribution is sub-leading in the powers of weak disorder strength $\alpha \ll 1$ as

long as the Fermi energy lies outside the gap. Similarly, the AA and RR bubbles in the expression of s_α^I are sub-leading and may be neglected. Furthermore, we work in the zero temperature limit.

The linear response to electric field and time derivative of magnetization corresponds to $V_{\mathbf{q},\omega} = -\hat{\mathbf{j}} \cdot \mathbf{A} - \Delta_{\text{sd}} \mathbf{m} \cdot \boldsymbol{\sigma}$, so that we obtain

$$s_{\mathbf{q},\omega} = \frac{1}{v^2 \hbar} \hat{\mathbf{K}}(\mathbf{q}, \omega) [\text{ev}(\mathbf{E}_{\mathbf{q},\omega} \times \hat{\mathbf{z}}) - i\omega \Delta_{\text{sd}} \mathbf{m}_\omega], \quad (1.28)$$

where the components of the tensor $\hat{\mathbf{K}}$ are given by

$$\hat{K}_{\alpha\beta}(\mathbf{q}, \omega) = v^2 \int \frac{d^2 \mathbf{p}}{(2\pi)^2} \text{Tr} \langle \sigma_\alpha G_{\mathbf{p}+\hbar\mathbf{q}, \varepsilon+\hbar\omega}^R \sigma_\beta G_{\mathbf{p}, \varepsilon}^A \rangle. \quad (1.29)$$

Eqs. (1.28,1.29) correspond to Eqs. (1.6,3.24) of the main text. Here we used the expression for the current operator $\hat{\mathbf{j}} = v_f(\boldsymbol{\sigma} \times \hat{\mathbf{z}})$ and electric field $\mathbf{E}_{\mathbf{q},\omega} = i\omega \mathbf{A}_{\mathbf{q},\omega}$.

1.2 CALCULATION OF THE SPIN-SPIN CORRELATOR

We shall compute the matrix $\hat{\mathbf{M}}$ to the second order in powers of ω and \mathbf{q} . The result is represented as

$$\mathbf{M} = \mathbf{M}_0 + \mathbf{M}_\omega + \mathbf{M}_{\omega^2} + \mathbf{M}_{q\omega} + \mathbf{M}_{q^2}, \quad (1.30a)$$

$$\mathbf{M}_0 = \frac{1}{\pi\alpha(\varepsilon^2 + \Delta_z^2)} \begin{pmatrix} \varepsilon^2 & 0 & 0 & -\varepsilon\Delta_z \\ 0 & (\varepsilon^2 - \Delta_z^2)/2 & \pi\alpha\varepsilon\Delta_z & 0 \\ 0 & -\pi\alpha\varepsilon\Delta_z & (\varepsilon^2 - \Delta_z^2)/2 & 0 \\ -\varepsilon\Delta_z & 0 & 0 & \Delta_z^2 \end{pmatrix}, \quad (1.30b)$$

$$\mathbf{M}_\omega = \frac{i\omega\varepsilon}{[\pi\alpha(\varepsilon^2 + \Delta_z^2)]^2} \begin{pmatrix} \varepsilon^2 & 0 & 0 & -\varepsilon\Delta_z \\ 0 & (\varepsilon^2 - \Delta_z^2)/2 & \pi\alpha(\varepsilon^2 - \Delta_z^2)\Delta_z/2\varepsilon & 0 \\ 0 & -\pi\alpha(\varepsilon^2 - \Delta_z^2)\Delta_z/2\varepsilon & (\varepsilon^2 - \Delta_z^2)/2 & 0 \\ -\varepsilon\Delta_z & 0 & 0 & \Delta_z^2 \end{pmatrix}, \quad (1.30c)$$

$$\mathbf{M}_{\omega^2} = \frac{(i\omega\varepsilon)^2}{[\pi\alpha(\varepsilon^2 + \Delta_z^2)]^3} \begin{pmatrix} \varepsilon^2 & 0 & 0 & -\varepsilon\Delta_z \\ 0 & (\varepsilon^2 - \Delta_z^2)/2 & \pi\alpha(\varepsilon^2 - \Delta_z^2)\Delta_z/2\varepsilon & 0 \\ 0 & -\pi\alpha(\varepsilon^2 - \Delta_z^2)\Delta_z/2\varepsilon & (\varepsilon^2 - \Delta_z^2)/2 & 0 \\ -\varepsilon\Delta_z & 0 & 0 & \Delta_z^2 \end{pmatrix}, \quad (1.30d)$$

$$\mathbf{M}_{q\omega} = \frac{v(\varepsilon^2 - \Delta_z^2)}{[\pi\alpha(\varepsilon^2 + \Delta_z^2)]^2} \left(\frac{-i}{2} + \frac{\varepsilon\omega}{[\pi\alpha(\varepsilon^2 + \Delta_z^2)]} \right) \begin{pmatrix} 0 & \varepsilon q_x & \varepsilon q_y & 0 \\ \varepsilon q_x & 0 & 0 & -\Delta_z q_x \\ \varepsilon q_y & 0 & 0 & -\Delta_z q_y \\ 0 & -\Delta_z q_x & -\Delta_z q_y & 0 \end{pmatrix}, \quad (1.30e)$$

$$\mathbf{M}_{q^2} = \frac{v^2(\varepsilon^2 - \Delta_z^2)}{2[\pi\alpha(\varepsilon^2 + \Delta_z^2)]^3} \begin{pmatrix} \varepsilon^2 q^2 & 0 & 0 \\ 0 & -(\varepsilon^2 - \Delta_z^2)(3q_x^2 - q_y^2)/4 & -(\varepsilon^2 - \Delta_z^2)q_x q_y/2 \\ 0 & -(\varepsilon^2 - \Delta_z^2)q_x q_y/2 & -(\varepsilon^2 - \Delta_z^2)(3q_y^2 - q_x^2)/4 \\ -\varepsilon\Delta_z q^2 & 0 & 0 \end{pmatrix}, \quad (1.30f)$$

from which the components of $\hat{\mathbf{K}}$ are obtained. Complete expressions for the components are cumbersome, therefore we proceed by first analyzing their denominator, which is proportional to $\det[1 - \pi\alpha\mathbf{M}]$

$$\begin{aligned} \det[1 - \pi\alpha M] = & -\frac{\varepsilon (\varepsilon^2 + 3\Delta_z^2)^2}{4\pi\alpha (\varepsilon^2 + \Delta_z^2)^3} \times \left(i\omega \left(1 - i\omega\tau_{\text{tr}} \frac{\varepsilon^2 - 5\Delta_z^2}{\varepsilon^2 - \Delta_z^2} + \mathcal{O}((\omega\tau_{\text{tr}})^2) \right) \right. \\ & \left. - Dq^2 \left(1 + i\omega\tau_{\text{tr}} \frac{13\Delta_z^4 + 10\Delta_z^2\varepsilon^2 + \varepsilon^4}{(\varepsilon^2 - \Delta_z^2)(\varepsilon^2 + \Delta_z^2)} - (i\omega\tau_{\text{tr}})^2 \frac{(\varepsilon^2 + 3\Delta_z^2)(\varepsilon^4 - 14\varepsilon^2\Delta_z - 35\Delta_z^4)}{(\varepsilon^2 - \Delta_z^2)(\varepsilon^2 + \Delta_z^2)} + \mathcal{O}((\omega\tau_{\text{tr}})^3) \right) \right) \end{aligned}$$

By restricting ourselves to perturbations that vary slow in time compared to the transport time τ_{tr} and smooth in space compared to the diffusion length $L_D = \sqrt{D\tau_{\text{tr}}}$, i.e. $\omega\tau_{\text{tr}}, Dq^2\tau_{\text{tr}} \ll 1$, we are able to extract the diffusion pole $(i\omega - Dq^2)^{-1}$.

The components of the conductivity tensor $\hat{\sigma}$ at finite ω and q are given by

$$\begin{aligned} \sigma_{xx} = & \sigma_0 + \frac{Dq^2}{i\omega - Dq^2} \left(\frac{q_y^2}{q^2} \sigma_0 \right. \\ & \left. - i\omega\tau_{\text{tr}} \left(\frac{2}{\pi\alpha} \frac{\varepsilon^2 + 2\Delta_z^2}{\varepsilon^2 + \Delta_z^2} + \frac{3}{\pi\alpha} \frac{q_x^2 - q_y^2}{2q^2} \right) \right) \end{aligned} \quad (1.32a)$$

$$\begin{aligned} \sigma_{yy} = & \sigma_0 + \frac{Dq^2}{i\omega - Dq^2} \left(\frac{q_x^2}{q^2} \sigma_0 \right. \\ & \left. - i\omega\tau_{\text{tr}} \left(\frac{2}{\pi\alpha} \frac{\varepsilon^2 + 2\Delta_z^2}{\varepsilon^2 + \Delta_z^2} - \frac{3}{\pi\alpha} \frac{q_x^2 - q_y^2}{2q^2} \right) \right) \end{aligned} \quad (1.32b)$$

$$\sigma_{xy} = \sigma_H + \frac{Dq^2}{i\omega - Dq^2} \left(-\frac{q_x q_y}{q^2} \sigma_0 - i\omega\tau_{\text{tr}} \frac{3}{\pi\alpha} \frac{q_x q_y}{q^2} \right) \quad (1.32c)$$

$$\sigma_{yx} = -\sigma_H + \frac{Dq^2}{i\omega - Dq^2} \left(-\frac{q_x q_y}{q^2} \sigma_0 - i\omega\tau_{\text{tr}} \frac{3}{\pi\alpha} \frac{q_x q_y}{q^2} \right), \quad (1.32d)$$

where σ_0 and σ_H are given in Eq. (1.9) of the main text. The remaining components of \hat{K} are given by

$$Q = \frac{\Delta_z}{v} \frac{iDq}{i\omega - Dq^2} \left(1 + i\omega\tau_{\text{tr}} \frac{(\varepsilon^2 + 7\Delta_z^2)}{\varepsilon^2 + \Delta_z^2} \right), \quad (1.33a)$$

$$\zeta = \frac{\Delta_z^2}{\varepsilon} \frac{1 - i\omega\tau_{\text{tr}}(\varepsilon^2 - 5\Delta_z^2)/(\varepsilon^2 - \Delta_z^2)}{i\omega - Dq^2 + \omega^2\tau_{\text{tr}}(\varepsilon^2 - 5\Delta_z^2)/(\varepsilon^2 - \Delta_z^2)}, \quad (1.33b)$$

where the ω^2 -term was included in the denominator of ζ because of its importance when taking the limit $q \rightarrow 0$. The leading contributions to Eq. (1.33a) in the limit $\omega\tau_{\text{tr}} \ll 1$ together with Eq. (1.33b) in the limit $q \rightarrow 0$ corresponds to Eqs. (1.8,1.9,1.15) of the main text.

It is convenient to rotate the coordinate system such that the new \hat{x} axis lies along \mathbf{q} . Let us introduce a rotation matrix \mathbf{U} to transform the tensor $\hat{\mathbf{K}}$,

$$\mathbf{U} = \begin{pmatrix} q_x/q & -q_y/q & 0 \\ q_y/q & q_x/q & 0 \\ 0 & 0 & 1 \end{pmatrix}, \quad \tilde{\mathbf{K}} = \mathbf{U}^\top \hat{\mathbf{K}} \mathbf{U}, \quad (1.34)$$

so that the new components of Eqs. (1.32) become

$$\tilde{\sigma}_{xx} = \sigma_0 - \frac{Dq^2}{i\omega - Dq^2} i\omega\tau_{\text{tr}} \frac{7\varepsilon^2 + 11\Delta_z^2}{2\pi\alpha(\varepsilon^2 + \Delta_z^2)} \quad (1.35a)$$

$$\tilde{\sigma}_{yy} = \sigma_0 + \frac{Dq^2}{i\omega - Dq^2} \left(\sigma_0 - i\omega\tau_{\text{tr}} \frac{\varepsilon^2 + 5\Delta_z^2}{2\pi\alpha(\varepsilon^2 + \Delta_z^2)} \right) \quad (1.35b)$$

$$\tilde{\sigma}_{yx} = -\tilde{\sigma}_{xy} = \sigma_H, \quad (1.35c)$$

and the rotated, $\tilde{\mathbf{K}}$, tensor is conveniently written as

$$\tilde{\mathbf{K}} = \begin{pmatrix} \tilde{\sigma}_{xx} & \sigma_H & 0 \\ -\sigma_H & \tilde{\sigma}_{yy} & Q \\ 0 & Q & \zeta \end{pmatrix}. \quad (1.36)$$

1.3 LIMITING BEHAVIOR OF $\mathbf{M}(\mathbf{T})$

To illustrate the behavior of $\mathbf{m}(\mathbf{t})$ we consider $f = f_0 \cos(\omega t)$ at a particular point \mathbf{r} . It is, also, convenient to let the field \mathbf{H}_{eff} to lie in the $\hat{x} - \hat{z}$ -plane and rotate the coordinate system such that \mathbf{H}_{eff} lies along new z -direction. This is achieved by introducing the rotation matrix $\hat{\mathbf{R}}$,

$$\hat{\mathbf{R}} = \begin{pmatrix} \cos \chi & 0 & -\sin \chi \\ 0 & 1 & 0 \\ \sin \chi & 0 & \cos \chi \end{pmatrix}, \quad (1.37)$$

where χ is the angle between \hat{z} and \mathbf{H}_{eff} . Furthermore, introducing the frequency $\omega_0 = |\gamma \mathbf{H}_{\text{eff}}|$ and the unit vector $\hat{\mathbf{h}} = (-\sin \chi, 0, \cos \chi)^\top$, we can write the equation of motion in the rotated coordinate frame as

$$\begin{aligned} \partial_t \mathbf{m} = & -\omega_0 \mathbf{m} \times \hat{\mathbf{z}} + f(\mathbf{r}, t) (\mathbf{m} \cdot \hat{\mathbf{h}}) [\mathbf{m} \times \hat{\mathbf{h}}] \\ & + \alpha_G [\mathbf{m} \times (\partial_t \mathbf{m})] - \alpha_G (\partial_t \mathbf{m}) \cdot \hat{\mathbf{z}} [\mathbf{m} \times \hat{\mathbf{z}}], \end{aligned} \quad (1.38)$$

where the vector $\hat{\mathbf{z}}$ is defined now as the unit vector along \mathbf{H}_{eff} , hence the magnetization projection $m_H = \mathbf{m} \cdot \hat{\mathbf{h}}$ is simply given by m_z .

In the regime of $\alpha_G \ll f_0 \ll \omega_0$ we can find the asymptotic behavior of m_H at sufficiently small times. In order to do that it is convenient to represent \mathbf{m} in spherical coordinates: $\mathbf{m} = (\sin \theta \cos \phi, \sin \theta \sin \phi, \cos \theta)^\top$, where θ is the polar angle between \mathbf{m} and \hat{z} and ϕ is the azimuth. In the limit $\alpha_G \rightarrow 0$ we find the equations of motion on θ and ϕ :

$$\partial_t \theta = \sin \chi \sin \phi f(r, t) (\sin \chi \sin \theta \cos \phi - \cos \chi \cos \theta) \quad (1.39)$$

$$\begin{aligned} \partial_t \phi = \omega_0 + f(r, t) \cos \theta & (\cos^2 \chi \cos^2 \phi - \sin^2 \phi \\ & - \frac{1}{2} \sin \chi (\cot \theta - \sin \theta)). \end{aligned} \quad (1.40)$$

We take $f(r, t) = f_0 \cos \omega t$ and assume that $f_0 \ll \omega_0$, so that we find $\phi = \omega_0 t - \phi_0$. It is convenient to choose $\phi_0 = \pi/2$ so that

$$\partial_t \theta = -f_0 \sin \chi \cos^2 \omega_0 t (\sin \theta \sin \chi \sin \omega_0 t - \cos \theta \cos \chi). \quad (1.41)$$

Because we assumed that $f_0 \ll \omega_0$, the dynamics of ϕ is much faster than the dynamics of θ . Therefore we average Eq. (1.41) over ϕ and obtain

$$\partial_t \theta = \frac{f_0}{4} \cos \theta \sin 2\chi. \quad (1.42)$$

This equation is readily solved by means of the substitution $\cos \theta = 1/\cosh x$, $\sin \theta = -\tanh x$. Using the initial condition $\theta(0) = 0$ one finds

$$\cos \theta(t) = \frac{1}{\cosh \left(\frac{1}{4} f_0 t \sin 2\chi \right)}, \quad (1.43)$$

which gives the result of Eq. (1.19) of the main text.

BIBLIOGRAPHY

- [Miron *et al.*(2010)Miron, Gaudin, Auffret, Rodmacq, Schuhl, Pizzini, Vogel, and Gambardella] I. M. Miron, G. Gaudin, S. Auffret, B. Rodmacq, A. Schuhl, S. Pizzini, J. Vogel, and P. Gambardella, *Nature Materials* **9**, 230 (2010).
- [Haney *et al.*(2013)Haney, Lee, Lee, Manchon, and Stiles] P. M. Haney, H.-W. Lee, K.-J. Lee, A. Manchon, and M. D. Stiles, *Phys. Rev. B* **87** (2013), 10.1103/PhysRevB.87.174411.
- [Dyakonov and Perel(1971)] M. I. Dyakonov and V. I. Perel, *Physics Letters A* **35**, 459 (1971).
- [Awschalom and Samarth(2009)] D. Awschalom and N. Samarth, *Physics* **2**, 50 (2009).
- [Manchon and Zhang(2008)] A. Manchon and S. Zhang, *Phys. Rev. B* **78** (2008), 10.1103/PhysRevB.78.212405.
- [Garate and MacDonald(2009)] I. Garate and A. H. MacDonald, *Phys. Rev. B* **80** (2009), 10.1103/PhysRevB.80.134403.
- [Manchon and Zhang(2009)] A. Manchon and S. Zhang, *Physical Review B* **79**, 094422 (2009).
- [Slonczewski(1996)] J. C. Slonczewski, *J. Magn. Magn. Mater.* **159**, L1 (1996).
- [Berger(1996)] L. Berger, *Phys. Rev. B* **54**, 9353 (1996).
- [Ralph and Stiles(2008)] D. Ralph and M. Stiles, *Journal of Magnetism and Magnetic Materials* **320**, 1190 (2008).
- [Stiles and Zangwill(2002)] M. D. Stiles and A. Zangwill, *Physical Review B* **66**, 014407 (2002).
- [Fu *et al.*(2007)Fu, Kane, and Mele] L. Fu, C. L. Kane, and E. J. Mele, *Physical Review Letters* **98**, 106803 (2007).
- [Moore and Balents(2007)] J. E. Moore and L. Balents, *Physical Review B* **75**, 121306 (2007).
- [Roy(2009)] R. Roy, *Physical Review B* **79**, 195322 (2009).

- [Hsieh *et al.*(2008)Hsieh, Qian, Wray, Xia, Hor, Cava, and Hasan] D. Hsieh, D. Qian, L. Wray, Y. Xia, Y. S. Hor, R. J. Cava, and M. Z. Hasan, *Nature* **452**, 970 (2008).
- [Qi *et al.*(2008a)Qi, Hughes, and Zhang] X.-L. Qi, T. L. Hughes, and S.-C. Zhang, *Nature Physics* **4**, 273 (2008a).
- [Mellnik *et al.*(2014)Mellnik, Lee, Richardella, Grab, Mintun, Fischer, Vaezi, Manchon, Kim, S. A. R. Mellnik, J. S. Lee, A. Richardella, J. L. Grab, P. J. Mintun, M. H. Fischer, A. Vaezi, A. Manchon, E.-A. Kim, N. Samarth, and D. C. Ralph, *Nature* **511**, 449 (2014).
- [Wang *et al.*(2015)Wang, Deorani, Banerjee, Koirala, Brahlek, Oh, and Yang] Y. Wang, P. Deorani, K. Banerjee, N. Koirala, M. Brahlek, S. Oh, and H. Yang, *Phys. Rev. Lett.* **114**, 257202 (2015).
- [Fan *et al.*(2014)Fan, Upadhyaya, Kou, Lang, Takei, Wang, Tang, He, Chang, Montazeri, Yu, J. Y. Fan, P. Upadhyaya, X. Kou, M. Lang, S. Takei, Z. Wang, J. Tang, L. He, L.-T. Chang, M. Montazeri, G. Yu, W. Jiang, T. Nie, R. N. Schwartz, Y. Tserkovnyak, and K. L. Wang, *Nature Materials* **13**, 699 (2014).
- [Fan *et al.*(2016)Fan, Kou, Upadhyaya, Shao, Pan, Lang, Che, Tang, Montazeri, Murata, Chan, Y. Fan, X. Kou, P. Upadhyaya, Q. Shao, L. Pan, M. Lang, X. Che, J. Tang, M. Montazeri, K. Murata, L.-T. Chang, M. Akyol, G. Yu, T. Nie, K. L. Wong, J. Liu, Y. Wang, Y. Tserkovnyak, and K. L. Wang, *Nature Nanotechnology* **11**, 352 EP (2016).
- [Yasuda *et al.*(2017)Yasuda, Tsukazaki, Yoshimi, Kondou, Takahashi, Otani, Kawasaki, and Tokura] K. Yasuda, A. Tsukazaki, R. Yoshimi, K. Kondou, K. S. Takahashi, Y. Otani, M. Kawasaki, and Y. Tokura, *Phys. Rev. Lett.* **119**, 137204 (2017).
- [Cha *et al.*(2018)Cha, Noh, Kim, Son, Bae, Lee, Kim, Lee, Shin, Sim, Yang, Lee, Shim, Lee, Jo, S. Cha, M. Noh, J. Kim, J. Son, H. Bae, D. Lee, H. Kim, J. Lee, H.-S. Shin, S. Sim, S. Yang, S. Lee, W. Shim, C.-H. Lee, M.-H. Jo, J. S. Kim, D. Kim, and H. Choi, *Nature Nanotechnology* (2018), 10.1038/s41565-018-0195-y.
- [Liu *et al.*(2011)Liu, Moriyama, Ralph, and Buhrman] L. Liu, T. Moriyama, D. C. Ralph, and R. A. Buhrman, *Phys. Rev. Lett.* **106**, 036601 (2011).
- [Akyol *et al.*(2015)Akyol, Yu, Alzate, Upadhyaya, Li, Wong, Ekicibil, Khalili Amiri, and Wang] M. Akyol, G. Yu, J. G. Alzate, P. Upadhyaya, X. Li, K. L. Wong, A. Ekicibil, P. Khalili Amiri, and K. L. Wang, *Applied Physics Letters* **106**, 162409 (2015), <https://doi.org/10.1063/1.4919108>.

- [MacNeill *et al.*(2016)MacNeill, Stiehl, Guimaraes, Buhrman, Park, and Ralph] D. MacNeill, G. M. Stiehl, M. H. D. Guimaraes, R. A. Buhrman, J. Park, and D. C. Ralph, *Nature Physics* **13**, 300 EP (2016).
- [Guimaraes *et al.*(2018)Guimaraes, Stiehl, MacNeill, Reynolds, and Ralph] M. H. D. Guimaraes, G. M. Stiehl, D. MacNeill, N. D. Reynolds, and D. C. Ralph, *Nano Letters* **18**, 1311 (2018), pMID: 29328662, <https://doi.org/10.1021/acs.nanolett.7b04993> .
- [Sakai and Kohno(2014)] A. Sakai and H. Kohno, *Physical Review B* **89** (2014), 10.1103/PhysRevB.89.165307.
- [Ndiaye *et al.*(2017)Ndiaye, Akosa, Fischer, Vaezi, Kim, and Manchon] P. B. Ndiaye, C. A. Akosa, M. H. Fischer, A. Vaezi, E.-A. Kim, and A. Manchon, *Physical Review B* **96** (2017), 10.1103/PhysRevB.96.014408.
- [Burkov and Hawthorn(2010)] A. A. Burkov and D. G. Hawthorn, *Physical Review Letters* **105**, 066802 (2010).
- [Taguchi *et al.*(2015)Taguchi, Shintani, and Tanaka] K. Taguchi, K. Shintani, and Y. Tanaka, *Physical Review B* **92** (2015), 10.1103/PhysRevB.92.035425.
- [Shintani *et al.*(2016)Shintani, Taguchi, Tanaka, and Kawaguchi] K. Shintani, K. Taguchi, Y. Tanaka, and Y. Kawaguchi, *Physical Review B* **93**, 195415 (2016).
- [Vonsovsky(1974)] S. V. Vonsovsky, *Magnetism* (Wiley, New York, 1974).
- [Ghosh and Manchon(2018)] S. Ghosh and A. Manchon, *Phys. Rev. B* **97**, 134402 (2018).
- [Maleev and Toperverg(1975)] S. Maleev and B. Toperverg, *Zh. Eksp. Teor. Fiz* **69**, 1440 (1975).
- [Maleev and Toperverg(1976)] S. Maleev and B. Toperverg, *Soviet Journal of Experimental and Theoretical Physics* **42**, 734 (1976).
- [Altshuler and Aronov(1985)] B. Altshuler and A. G. Aronov, *Amsterdam: North-Holland* p **1**, 155 (1985).
- [Ado *et al.*(2015)Ado, Dmitriev, Ostrovsky, and Titov] I. A. Ado, I. A. Dmitriev, P. M. Ostrovsky, and M. Titov, *EPL (Europhysics Letters)* **111**, 37004 (2015).
- [Ado *et al.*(2016)Ado, Dmitriev, Ostrovsky, and Titov] I. A. Ado, I. A. Dmitriev, P. M. Ostrovsky, and M. Titov, *Phys. Rev. Lett.* **117**, 046601 (2016).

- [Ado *et al.*(2017)Ado, Dmitriev, Ostrovsky, and Titov] I. A. Ado, I. A. Dmitriev, P. M. Ostrovsky, and M. Titov, Phys. Rev. B **96**, 235148 (2017).
- [Kong *et al.*(2011)Kong, Cha, Lai, Peng, Analytis, Meister, Chen, Zhang, Fisher, Shen, and Cui] D. Kong, J. J. Cha, K. Lai, H. Peng, J. G. Analytis, S. Meister, Y. Chen, H.-J. Zhang, I. R. Fisher, Z.-X. Shen, and Y. Cui, ACS Nano **5**, 4698 (2011).
- [Kamboj *et al.*(2017)Kamboj, Singh, Ferrus, Beere, Duffy, Hesjedal, Barnes, and Ritchie] V. S. Kamboj, A. Singh, T. Ferrus, H. E. Beere, L. B. Duffy, T. Hesjedal, C. H. W. Barnes, and D. A. Ritchie, ACS Photonics **4**, 2711 (2017).
- [Huang *et al.*(2017)Huang, Huang, Hsu, Wadekar, Yan, Yu, and Chou] S.-M. Huang, S.-J. Huang, C. Hsu, P. V. Wadekar, Y.-J. Yan, S.-H. Yu, and M. Chou, Scientific Reports **7** (2017), 10.1038/s41598-017-05369-y.
- [Xiang *et al.*(2014)Xiang, Wang, and Dou] F. X. Xiang, X. L. Wang, and S. X. Dou, arXiv:1401.6732 [cond-mat] (2014), arXiv: 1401.6732.
- [van der Bijl and Duine(2012)] E. van der Bijl and R. A. Duine, Phys. Rev. B **86**, 094406 (2012).
- [Hals and Brataas(2013)] K. M. D. Hals and A. Brataas, Phys. Rev. B **88**, 085423 (2013).
- [Tserkovnyak and Wong(2009)] Y. Tserkovnyak and C. H. Wong, Phys. Rev. B **79**, 014402 (2009).
- [Mahfouzi *et al.*(2012)Mahfouzi, Nagaosa, and Nikolić] F. Mahfouzi, N. Nagaosa, and B. K. Nikolić, Physical Review Letters **109** (2012), 10.1103/PhysRevLett.109.166602.
- [Ferreiros *et al.*(2015)Ferreiros, Buijnsters, and Katsnelson] Y. Ferreiros, F. J. Buijnsters, and M. I. Katsnelson, Phys. Rev. B **92**, 085416 (2015).
- [Fischer *et al.*(2016)Fischer, Vaezi, Manchon, and Kim] M. H. Fischer, A. Vaezi, A. Manchon, and E.-A. Kim, Physical Review B **93** (2016), 10.1103/PhysRevB.93.125303, arXiv:1305.1328 .
- [Yokoyama *et al.*(2010)Yokoyama, Zang, and Nagaosa] T. Yokoyama, J. Zang, and N. Nagaosa, Physical Review B **81** (2010), 10.1103/PhysRevB.81.241410.
- [Yokoyama(2011)] T. Yokoyama, Physical Review B **84**, 113407 (2011).
- [Siu *et al.*(2016)Siu, Son, Jalil, and Tan] Z. B. Siu, H. C. Son, M. b. A. Jalil, and S. G. Tan, arXiv:1609.02242 [cond-mat] (2016), arXiv:1609.02242 [cond-mat] .

- [Mahfouzi *et al.*(2016)Mahfouzi, Nikolić, and Kioussis] F. Mahfouzi, B. K. Nikolić, and N. Kioussis, *Physical Review B* **93** (2016), 10.1103/PhysRevB.93.115419.
- [Soleimani *et al.*(2017)Soleimani, Jalili, Mahfouzi, and Kioussis] M. Soleimani, S. Jalili, F. Mahfouzi, and N. Kioussis, *EPL (Europhysics Letters)* **117**, 37001 (2017).
- [Kurebayashi and Nomura(2017)] D. Kurebayashi and K. Nomura, arXiv:1702.04918 [cond-mat] (2017), arXiv:1702.04918 [cond-mat] .
- [Chen *et al.*(2017)Chen, Peng, and Zhou] J. Chen, Y. Peng, and J. Zhou, *Journal of Magnetism and Magnetic Materials* **432**, 554 (2017).
- [Rodriguez-Vega *et al.*(2016)Rodriguez-Vega, Schwiete, Sinova, and Rossi] M. Rodriguez-Vega, G. Schwiete, J. Sinova, and E. Rossi, arXiv:1610.04229 [cond-mat] (2016), arXiv:1610.04229 [cond-mat] .
- [Qi *et al.*(2008b)Qi, Hughes, and Zhang] X.-L. Qi, T. L. Hughes, and S.-C. Zhang, *Physical Review B* **78**, 195424 (2008b).
- [Garate and Franz(2010)] I. Garate and M. Franz, *Physical Review Letters* **104**, 146802 (2010).
- [Nomura and Nagaosa(2010)] K. Nomura and N. Nagaosa, *Physical Review B* **82**, 161401 (2010).
- [Tserkovnyak and Loss(2012)] Y. Tserkovnyak and D. Loss, *Physical Review Letters* **108** (2012), 10.1103/PhysRevLett.108.187201.
- [Linder(2014)] J. Linder, *Physical Review B* **90**, 041412 (2014).
- [Tserkovnyak *et al.*(2015)Tserkovnyak, Pesin, and Loss] Y. Tserkovnyak, D. A. Pesin, and D. Loss, *Physical Review B* **91**, 041121 (2015).
- [Ueda *et al.*(2012)Ueda, Takeuchi, Tatara, and Yokoyama] H. T. Ueda, A. Takeuchi, G. Tatara, and T. Yokoyama, *Physical Review B* **85**, 115110 (2012).
- [Liu and Sinova(2013)] X. Liu and J. Sinova, *Physical Review Letters* **111**, 166801 (2013).
- [Chang *et al.*(2015)Chang, Markussen, Smidstrup, Stokbro, and Nikolić] P.-H. Chang, T. Markussen, S. Smidstrup, K. Stokbro, and B. K. Nikolić, *Physical Review B* **92**, 201406 (2015).

- [Fujimoto and Kohno(2014)] J. Fujimoto and H. Kohno, Physical Review B **90**, 214418 (2014).
- [Okuma and Ogata(2016)] N. Okuma and M. Ogata, Physical Review B **93**, 140205 (2016).
- [Rammer and Smith(1986)] J. Rammer and H. Smith, Reviews of Modern Physics **58**, 323 (1986).

SPIN-ORBIT TORQUES IN RASHBA HONEYCOMB
ANTIFERROMAGNETS

Recent experiments on switching antiferromagnetic domains by electric current pulses have attracted a lot of attention to spin-orbit torques in antiferromagnets. In this work, we employ the tight-binding model solver, kwant, to compute spin-orbit torques in a two-dimensional antiferromagnet on a honeycomb lattice with strong spin-orbit interaction of Rashba type. Our model combines spin-orbit interaction, local s-d-like exchange, and scattering of conduction electrons on on-site disorder potential to provide a microscopic mechanism for angular momentum relaxation. We consider two versions of the model: one with preserved and one with broken sublattice symmetry. A non-equilibrium staggered polarization, that is responsible for the so-called Néel spin-orbit torque, is shown to vanish identically in the symmetric model but may become finite if sublattice symmetry is broken. Similarly, anti-damping spin-orbit torques vanish in the symmetric model but become finite and anisotropic in a model with broken sublattice symmetry. As expected, anti-damping torques also reveal a sizable dependence on impurity concentration. Our numerical analysis also confirms symmetry classification of spin-orbit torques and strong torque anisotropy due to in-plane confinement of electron momenta.

2.1 INTRODUCTION

Ferromagnetic spintronics has greatly contributed to microelectronic technology in the last few decades [Bader2010, Sinova2012, Bhatti2017]. One of the practical results was the development of magnetic memories with purely electronic write-in and read-out processes as an alternative to existing solid state drive technologies [Kent2015, Sato2018]. An increasing demand for ever higher performance computation and ever faster big data analytics has sparked recently the interest to antiferromagnetic spintronics [MacDonald2011, Gomonay2014, Wadley2016, Jungwirth2016AFMreview, Baltz2018, Jungwirth2018, Hoffman2018], i. e. to the usage of much more subtle antiferromagnetic order parameter to store and process information. This idea is driven primarily by the expectation that antiferromagnetic materials may naturally allow for up to THz operation frequencies [Gomonay2016AFM, Olejnik2018, Jungwirth2018] in sharp contrast to ferromagnets whose current-induced magnetization dynamics is fundamentally limited to GHz frequency range.

The best efficiency in electric switching of magnetic domains is achieved in systems involving materials with at least partial spin-momentum locking [Fina2016] due to sufficiently strong spin-orbit interaction. The latter is responsible for the so-called spin-orbit torques on magnetization that are caused by sizable non-equilibrium spin polarization induced by an electron flow [Brataas2012, Hals2013, Zelezny2014, 2014MokrousovSOT, Ghosh2017, SmejkalAFM_2017, Zelezny2018, Zhou2018, Manchon2018, Moriyama2018, Li2019, Chen2019, Zhou2019, Zhou2019a, Bodnar2018].

Recently, spin-orbit-torque-driven electric switching of the Néel vector orientation has been predicted [Zelezny2014] and discovered in non-centrosymmetric crystals such as CuMnAs [Wadley2016, Fina2016, Zelezny2018, Saidl2017] and Mn₂Au [Barthem2013, Jordan2015, Bhattacharjee2018]. Even though many antiferromagnetic compounds are electric insulators [Pandey2017], which limits the range of their potential applications, e. g., for spin injection [Tshitoyan2015], the materials like CuMnAs and Mn₂Au possess semi-metal and metal properties, inheriting strong spin-orbit coupling and sufficiently high conductivity. These materials also give rise to collective mode excitations in THz range [Bhattacharjee2018].

Spin-orbit torque in antiferromagnets have been investigated theoretically using Kubo-Streda formula in the case of two-dimensional (2D) Rashba gas, as well as in tight-binding models of Mn₂Au [Zelezny2014, Zelezny2017]. These pioneering works describe the spin-orbit torques based on their influence on the current-driven dynamics as predicted by Landau-Lifshitz-Gilbert equation. In particular, Zelezny et al. proposed that only a staggered field-like torque and an non-staggered anti-damping torque can trigger current-driven antiferromag-

Figure 2.1: Left panel (a): a two-dimensional honeycomb lattice hosting anti-parallel localized magnetic moments S^A and S^B that induce opposite exchange potentials on A and B sublattice. The vector d_{ij} is directed from an A-site i to one of the three nearest-neighbor B-sites j . Right panel (b): Fermi surfaces (strongly enlarged) in quasi-momentum space for the Fermi energy $E = 0.3t$, couplings $\lambda = 0.05t$, $\Delta = JS = 0.1t$, and $\theta = \pi/2$. Solid (orange) and dashed (green) lines indicate K and K' valleys.

netic THz switching and excitation in antiferromagnets (see e. g., Faerbu1995, Cheng2016, Khymyn2017). This analysis served as a basis to further investigation of spin-orbit torques in heterostructures [ManchonJPCM2017, Ghosh2017, Ghosh2019]. Furthermore, a symmetry group analysis has been developed to predict the form of these two components based on the magnetic point groups of the antiferromagnets [Zelezny2017, Watanabe2018].

In the context of current-driven antiferromagnetic domain wall [Hals2011] and skyrmion motion [Barker2016, Zhang2016], the Néel vector dynamics has been modeled within the phenomenological treatment of the Landau-Lifshitz-Gilbert equation pioneered by Slonczewski [SLONCZEWSKI1996]. In this phenomenological approach the torques on magnetization derived above have been simply postulated [Gomonay2016AFM, Shiino2016, Akosa2018, Tomasello2017].

While most of the above studies have focused on the existence and influence of the staggered field-like and non-staggered anti-damping torques, in the present work, we do compute all types of spin-orbit torques from a long-scale numerical analysis in a diffusive transport regime. Our study of spin-orbit torques is based on the numerical computation of non-equilibrium spin polarizations for an effective s-d type model in a two-dimensional (2D) honeycomb antiferromagnet with Rashba spin-orbit coupling and on-site disorder potential. Our results stress the importance of anisotropy of both field-like and anti-damping like spin-orbit torques due to 2D confinement of conduction electrons. We also find, surprisingly, that both the staggered field-like and non-staggered anti-damping torques vanish identically in a model with an s-d exchange coupling that is the same on two antiferromagnetic sublattices. In contrast, the model with strongly asymmetric s-d exchange couplings leads to finite anti-damping torques while the entire notion of staggered torques becomes largely irrelevant in such an asymmetric model.

2.2 MODEL

In this paper, we develop a numerical framework for the microscopic analysis of spin-orbit torques that is realized with the help of the tight-binding model solver, kwant [Groth2014]. Our methodology is illustrated using s-d type model for a

2D antiferromagnet on the honeycomb lattice depicted in Fig. 3.1a. To be more specific, we consider the Kane-Mele tight-binding model for conduction electrons [Kane2005, Qiao2012] with the Hamiltonian

$$H_0 = H_{\text{tb}} + H_{\text{R}} + H_{\text{sd}}, \quad (2.1)$$

where the first term describes the nearest-neighbor hopping,

$$H_{\text{tb}} = -t \sum_{\langle i,j \rangle} \sum_{\sigma} c_{i\sigma}^{\dagger} c_{j\sigma}, \quad (2.2)$$

with the hopping energy t . The operators $c_{i\sigma}^{\dagger}$ ($c_{i\sigma}$) are the standard creation (annihilation) operators for a fermion on the lattice site i with the spin index σ .

The term H_{R} describes spin-orbit interaction of Rashba type that is responsible for spin-orbit torque on magnetization. This spin-orbit interaction is represented by the term

$$H_{\text{R}} = \frac{i\lambda}{a} \sum_{\langle i,j \rangle} \sum_{\sigma\sigma'} \hat{z} \cdot (\boldsymbol{\sigma} \times \mathbf{d}_{ij})_{\sigma\sigma'} c_{i\sigma}^{\dagger} c_{j\sigma'}, \quad (2.3)$$

with the unit vector \hat{z} directed perpendicular to the 2D crystal plane. The notation $\boldsymbol{\sigma} = (\sigma_x, \sigma_y, \sigma_z)$ represents the three-dimensional vector of Pauli matrices, the vectors \mathbf{d}_{ij} connect neighboring sites as shown in Fig. 3.1a, and λ is the Rashba-spin-orbit strength. For any site i on the sublattice A we have three such vectors:

$$\mathbf{d}_1 = a \begin{pmatrix} 0 \\ 1 \end{pmatrix}, \quad \mathbf{d}_2 = \frac{a}{2} \begin{pmatrix} \sqrt{3} \\ -1 \end{pmatrix}, \quad \mathbf{d}_3 = -\frac{a}{2} \begin{pmatrix} \sqrt{3} \\ 1 \end{pmatrix}, \quad (2.4)$$

where a is the length of the bond between A and B.

Finally, the s - d -like exchange interaction between localized magnetic moments \mathbf{S}_i and spins of conduction electrons is described by the term

$$H_{\text{sd}} = -J \sum_i \sum_{\sigma\sigma'} \mathbf{S}_i \cdot \boldsymbol{\sigma}_{\sigma\sigma'} c_{i\sigma}^{\dagger} c_{i\sigma'}, \quad (2.5)$$

with the coupling strength J taken here to be the same on A and B sublattices. The term (3.1) couples the tight-binding model for conduction electrons to a classical Heisenberg model for localized angular momenta \mathbf{S}_i with antiferromagnetic ground state. The localized momenta \mathbf{S}_i are assumed to have large absolute value $|\mathbf{S}_i| = S \gg 1$. The characteristic s - d exchange energy is given by $\Delta = JS$. For conductivity and non-equilibrium spin density computations we assume the single-domain antiferromagnetic order, that is characterized by the unit Néel vector $\boldsymbol{\ell} = (\mathbf{S}^A - \mathbf{S}^B)/2S$.

Figure 2.2: The band structure cross-section at $k_y = 0$ for the model of Eq. (2.1) versus k_x counted with respect to the high-symmetry points \mathbf{K} and \mathbf{K}' for different orientations of the Néel vector, $\ell_z = \cos \theta$. Horizontal lines correspond to the Fermi energies $E = 0.0\text{ t}$, 0.05 t , and 0.3 t for which we perform the numerical analysis. For zero energy (band center), the system is insulating for $\theta > \pi/4$; for $\theta < \pi/4$ the Fermi energy crosses the conduction band in K valley and the valence band in \mathbf{K}' valley. For $E = 0.05\text{ t}$ all extended states belong to the conduction band in K valley that gives rise to 100% valley-polarization. For $E = 0.3\text{ t}$ both valleys contain two Fermi surfaces. The plots correspond to the parameters $\lambda = 0.05\text{ t}$ and $\Delta = 0.1\text{ t}$.

Equal exchange couplings on both sublattices in Eq. (3.1) and Rashba spin-orbit interaction of Eq. (2.3) ensure sublattice symmetry that greatly simplifies the results. In what follows we refer to the model as the symmetric model. At the end of the paper we also consider a more complex version of the model, where the sublattice symmetry is broken by a strong asymmetry of s-d couplings on A and B sublattices.

The model of Eq. (2.1) is motivated, in part, by the studies of CuMnAs [SmejkalAFM_2017]. A similar model was also used to describe silicene where circularly polarized light induces a staggered s-d-interaction [ezawa_photoinduced_2013]. The spin-orbit interaction of Eq. (2.3) breaks $\hat{z} \rightarrow -\hat{z}$ inversion symmetry. Similarly to CuMnAs we also assume that the Fermi energy of conduction electrons stay in a vicinity of the antiferromagnetic gap (or Dirac point). That means that the Fermi surfaces are located near two different pockets of the Brillouin zone – the so-called K and \mathbf{K}' valleys as shown in Fig. 3.1b (see also the caption in Fig. 3.2).

Due to the rather high symmetry of the model of Eqs. (2.1)-(3.1), the Fermi-surfaces remain entirely isotropic with respect to azimuthal (in-plane) direction of the Néel vector ℓ as illustrated in Fig. 3.1b. Still, the band-structure of the symmetric model depends strongly on the polar angle θ of the Néel vector, $\ell_z = \cos \theta$, as shown in Fig. 3.2.

From the microscopic point of view all spin-orbit torques (as well as spin-transfer torques, spin-orbit induced Gilbert damping and effective renormalization of angular momenta S_i) can be directly related to non-equilibrium contributions to the local spin density s_i that are proportional to electric current (or, in the case of Gilbert damping, to the time derivatives of the classical field S_i) [AdoSOT2017, AdoSTTGD2019]. The microscopic analysis of the torques is, therefore, similar to the microscopic analysis of the conductivity and must involve the mechanisms of momentum relaxation of conduction electrons that, in our system, is also directly related to the angular momentum relaxation of localized spins S_i . Here we model such a momentum relaxation by adding non-

Figure 2.3: Two-terminal geometry that is used for computation of spin-orbit torques. The largest sample corresponds to a wide zigzag nano-ribbon with $L \sim W \sim 750 a$. We assume periodic boundary conditions in y direction for both the sample and the leads. The sample is described by the model of Eq. (2.6) with on-site disorder potential $V_i = \pm V_d$. Left and right leads ($x < 0$ and $x > L$, respectively) are described by a clean Hamiltonian of Eq. (2.1). The non-equilibrium spin density per current flux (averaged over the entire sample) is defined by the linear response formula of Eq. (2.15).

magnetic on-site disorder potential to the model of Eq. (2.1). Namely, we consider an ensemble of tight-binding models

$$H = H_0 + \sum_i \sum_{\sigma\sigma'} V_i c_{i\sigma}^\dagger c_{i\sigma'} \quad (2.6)$$

where V_i are random on-site potentials on randomly selected sites. For numerical simulations we take $V_i = \pm V_d$ (with a random sign) on random lattice sites in the scattering region (the sample) as illustrated in Fig. 2.3. In various simulations we chose $V_d = 0.2 t$ and $V_d = 0.5 t$ and place impurities on 30%, 40% and 50% of the lattice sites in the sample. Each point is obtained by averaging over 30 – 80 disorder realizations.

Even though the spin-orbit torques are completely defined by the tight-binding model of Eq. (2.6), they are insufficient to describe magnetization dynamics of an antiferromagnet. The latter also depends on the type of the Heisenberg model used for S_i as well as on the Gilbert damping terms. In the presence of magnetic textures one should also take into account in-plane spin-transfer torques (which are defined by the response of spin density s_i to both electric current and spacial gradients of S_i). Intimate relations between all these seemingly different (and often highly anisotropic) quantities have recently been established for a 2D Rashba ferromagnet in the metal regime [AdoSTTGD2019].

2.3 SCATTERING APPROACH

In this paper we present a numerical analysis of spin-orbit torques using the scattering framework. The framework appeals to the two terminal geometry depicted schematically in Fig. 2.3. Left and right leads (reservoirs) are modeled by semi-infinite systems of the width W described by ballistic tight-binding model of Eq. (2.1) with periodic boundary conditions in y direction. For both leads one constructs left and right-going scattering states, $\Psi_{\alpha,E}^{L,\lessgtr}(r_i)$ and $\Psi_{\alpha,E}^{R,\lessgtr}(r_i)$, that are the eigenstates of the model of Eq. (2.1) that are normalized to the unit probability current flux through the lead cross-section.

The scattering states are labeled by (i) the eigenenergy E ; (ii) the lead index: L for the left lead and R for the right one; (iii) the flux direction: $>$ for the probability current in x direction and $<$ for the probability current in the opposite ($-x$) direction, and (iv) by a composite index $\alpha = (n, \sigma, \nu)$ that incorporates the channel index n (numerationing states with different projections of the wave vector on the transversal direction y), the spin projection σ and the band index ν numerating Fermi surfaces. Note that the dimension of the scattering state wave-function is $1/\sqrt{Wv_\alpha}$, where v_α is the x -component of the velocity in the channel α .

With the help of the scattering states one can readily formulate a scattering problem at a given energy E that is solved by the wave-function matching at the lead-sample interface for each disorder realization. For example, a scattering problem that corresponds to populating an incoming channel $\Psi_{\alpha,E}^{L,>}$ results in the eigenstate that has the following form in the leads

$$\Psi_{\alpha,E}^L(\mathbf{r}) = \begin{cases} \Psi_{\alpha,E}^{L,>}(\mathbf{r}) + \sum_{\beta} r_{\beta\alpha} \Psi_{\beta,E}^{L,<}(\mathbf{r}), & x < 0, \\ \sum_{\beta} t_{\beta\alpha} \Psi_{\beta,E}^{R,>}(\mathbf{r}), & x > L \end{cases}, \quad (2.7)$$

where $t_{\beta\alpha}$ and $r_{\beta\alpha}$ denote the so-called transmission and reflection amplitudes, correspondingly. Similarly, the scattering problem that corresponds to populating a left-going state in the right lead, $\Psi_{\alpha,E}^{R,<}$, corresponds to the eigenstate

$$\Psi_{\alpha,E}^R(\mathbf{r}) = \begin{cases} \sum_{\beta} t'_{\beta\alpha} \Psi_{\beta,E}^{L,<}(\mathbf{r}), & x < 0, \\ \Psi_{\alpha,E}^{R,<}(\mathbf{r}) + \sum_{\beta} r'_{\beta\alpha} \Psi_{\beta,E}^{R,>}(\mathbf{r}), & x > L \end{cases}. \quad (2.8)$$

The reflection and transmission amplitudes are organized into the scattering matrix

$$S = \begin{pmatrix} \hat{r} & \hat{t}' \\ \hat{t} & \hat{r}' \end{pmatrix} \quad (2.9)$$

that yields the unitarity constraint $S^\dagger S = 1$. The constraint is ensured by the normalization of the scattering states $\Psi_{\alpha,E}^{\geq}(\mathbf{r})$ to the unit probability current flux that is conserved for each energy E (in the absence of non-elastic processes).

The results of Eqs. (2.7)-(2.8) are routinely used to express, e.g. the time-averaged electric current flowing through the sample as

$$I = e \int \frac{dE}{2\pi\hbar} (f_R(E) - f_L(E)) \sum_{\alpha\beta} |t_{\alpha\beta}(E)|^2, \quad (2.10)$$

Figure 2.4: Averaged two-terminal conductivity $L\langle G\rangle/W$ for the symmetric coupling model computed from Eq. (2.11) as the function of the sample length L for several values of the Fermi energy E , impurity strength V_d and impurity concentration n_{imp} . Each point corresponds to averaging over 30 disorder realizations. The curves correspond to $\Delta = 0.1 t$, $\lambda = 0.05 t$ and $\theta = \pi/4$ and are fitted using Eq. (2.12). Similar behavior is observed for various angles θ .

where f_L and f_R stand for electron distribution functions in the left and right leads, respectively, and $e = -|e|$ is the electron charge. The expression for electric current leads to the celebrated [datta_1995] Landauer-Büttiker formula for the conductance

$$G = I/V_{\text{bias}} = \frac{e^2}{h} \sum_{\alpha\beta} |t_{\alpha\beta}(E)|^2, \quad (2.11)$$

where V_{bias} is the voltage bias between the left and right leads (that sets a difference between the chemical potentials in the leads: $\delta\mu = \mu_L - \mu_R = eV_{\text{bias}}$) and E is the average chemical potential in the sample (which we simply call the Fermi energy).

The dependence of the average conductance on the sample length (for $L \simeq W$) is then fitted by the following formula

$$\langle G \rangle_{\text{dis}} = \frac{2e^2}{h} \frac{W}{L + \ell_0} \sigma, \quad (2.12)$$

where the angular brackets stand for averaging over disorder realizations, while the constant σ is regarded as 2D dimensionless conductivity (which is independent of both L and W). The length scale ℓ_0 in Eq. (2.12) is of the order of the transport mean free path in the system.

The straightforward numerical analysis using kwant package [Groth2014] provides us with the two terminal conductivity, $L\langle G\rangle/W$, that is plotted in Fig. 2.4 for the metal regime ($E = 0.3 t$, left panel) and for the half-metal regime ($E = 0.05 t$, right panel). The metal regime refers here to the Fermi energies that correspond to two Fermi surfaces per valley, while the half-metal regime corresponds to a single Fermi surface. Similar plots are generated for various polar angles θ of the Néel vector. Both the 2D conductivity σ and the mean free path ℓ_0 are, then, extracted from the fitting formula of Eq. (2.12) and plotted in Fig. 2.5 as the function of $\ell_z = \cos \theta$. The estimate of ℓ_0 is necessary to ensure that our sample size is at least of the order of the mean free path to avoid non-universal finite-size effects in our data.

One can see from Fig. 2.5 that both the mean free path ℓ_0 and the conductivity σ are nearly constant in the metal regime. Their dependence on the Néel vector

Figure 2.5: The conductivity σ and the mean free path ℓ_0 in the symmetric coupling model of Eq. (2.6) as the function of the Néel vector orientation $\ell_z = \cos \theta$. Both quantities are extracted from our numerical data with the help of Eq. (2.12). Large variations of the mean free path in the half-metal regime are associated with the Fermi energy touching the band edge at certain polar angles of the Néel vector.

orientation is weak, which is consistent with the fact that such a dependence must disappear in the limit $E \gg \Delta$. In the half-metal regime, however, the conductivity is strongly dependent on both disorder concentration and the Néel vector angle θ . We will see below, that despite rather strong angular dependence of the conductivity, one of the field-like spin-orbit torques remains θ -independent in the half-metal regime.

For $E = 0$, the system exhibits metal-insulator transition as the function of the Néel vector orientation (see the second panel of Fig. 2.4). This choice of the Fermi energy leads, however, to vanishing spin-orbit torques as discussed below.

2.4 SPIN-ORBIT TORQUES

The package kwant [Groth2014] does not only provide the elements of the scattering matrix $S(E)$ in Eq. (2.9), but also gives access to the solutions $\Psi_{\alpha,E}^{L,R}(\mathbf{r})$ inside the sample. Such solutions can, therefore, be used to obtain a local expectation value of the electron spin (we refer here to the dimensionless spin defined by the operator $\boldsymbol{\sigma}/2$) as

$$\mathbf{s}(\mathbf{r}) = \frac{1}{2} \int \frac{dE}{2\pi\hbar} \sum_A f_A(E) \sum_{\alpha} \Psi_{\alpha,E}^A \dagger \boldsymbol{\sigma}_{\sigma\sigma'} \Psi_{\alpha,E}^A, \quad (2.13)$$

where $\alpha = (n, \sigma, v)$ and the index $A = L, R$ numerates the leads.

In order to extract spin-orbit torques we have to decompose the local electron spin to equilibrium and non-equilibrium contributions as

$$\mathbf{s}(\mathbf{r}) = \mathbf{s}_0(\mathbf{r}) + \delta\mathbf{s}(\mathbf{r}). \quad (2.14)$$

Equilibrium spin density, \mathbf{s}_0 , corresponds to the limit of zero bias (or thermal bias) $f_L = f_R = f(E)$, where $f(E)$ is the Fermi-Dirac distribution function. The quantity \mathbf{s}_0 describes equilibrium conduction electron contributions to the parameters of the Heisenberg model for localized momenta \mathbf{S}_i that we do not discuss here.

Non-equilibrium contribution, δs , describes the effects induced e. g. by a bias voltage, V_{bias} , such as the spin-orbit torques on magnetization. In the linear response we obtain, in the spirit of Eq. (2.11), the formula

$$\frac{\delta s(\mathbf{r})}{\delta \mu} = \frac{1}{4\hbar} \sum_{\alpha} \left[\Psi_{\alpha,E}^{\text{R}\dagger}(\mathbf{r}) \sigma_{\sigma\sigma'} \Psi_{\alpha,E}^{\text{R}}(\mathbf{r}) - \Psi_{\alpha,E}^{\text{L}\dagger}(\mathbf{r}) \sigma_{\sigma\sigma'} \Psi_{\alpha,E}^{\text{L}}(\mathbf{r}) \right], \quad (2.15)$$

where $\delta \mu = eV_{\text{bias}}$ and the scattering states are taken at the Fermi energy. Similarly to Eq. (2.11), we assume here that the quantities $\Psi_{\alpha,E}^{\text{A}\dagger} \sigma \Psi_{\alpha,E}^{\text{A}}$ have negligible energy dependence within the interval $\delta \mu$ around the Fermi energy.

In numerical simulations we systematically employ Eq. (2.15) to extract the spin density on A and B sublattices by varying the direction of the Néel vector. The results are fitted by the expansion of δs in angular harmonics that are compatible with the symmetry of the model. Before, we proceed with the discussion of our results let us pause to clarify the relation between the non-equilibrium spin-density and microscopic spin-orbit torques on magnetization that enter effective Landau-Lifshits-Gilbert (LLG) equation on magnetization dynamics.

2.5 MICROSCOPIC LLG EQUATION

The problem of magnetization dynamics can be formulated with the help of a Heisenberg model for the localized momenta \mathbf{S}_i that is coupled to a tight-binding model for conduction electrons by means of the local exchange interaction of Eq. (3.1). Depending on the type of the Heisenberg model we may obtain different equations of motion but the torques on magnetization (originating from electric current or field) and also Gilbert damping terms can be understood from the tight-binding Hamiltonian of Eq. (2.6) alone [AdoSTTGD2019].

For the sake of illustration let us outline the derivation of magnetization dynamics for a Heisenberg model of an “isotropic” antiferromagnet. The local interaction of Eq. (3.1) dictates the equation of motion of localized momenta of the form

$$\dot{\mathbf{S}}_i = \mathbf{H}_i \times \mathbf{S}_i + \frac{\mathbf{J}}{\hbar} \mathbf{S}_i \times \sum_{\sigma\sigma'} \langle c_{i\sigma}^{\dagger} \sigma_{\sigma\sigma'} c_{i\sigma'} \rangle, \quad (2.16)$$

where dot stands for the time derivative of \mathbf{S}_i and $\mathbf{H}_i = -\delta F / \delta \hbar \mathbf{S}_i$ is an effective field (in frequency units) on a site i that is defined by the free energy F of the classical Heisenberg model for localized spins. The angular brackets denote the thermodynamic expectation value of conduction electron spin operator on the same site i .

For a collinear antiferromagnet we shall distinguish two sublattices A and B that are characterized by opposite directions of the localized momenta $\mathbf{S}_i^A = -\mathbf{S}_i^B$ in the antiferromagnetic ground state. It is assumed, that these directions remain to be almost opposite even for out-of-equilibrium conditions. It is also natural to assume that, as far as the magnet is far from a phase transition, the classical fields \mathbf{S}_i^A and \mathbf{S}_i^B remain smooth on atomic scales. Below we consider a single domain antiferromagnet, which is characterized by two time-dependent unit vectors $\mathbf{n}^{A,B} = \mathbf{S}^{A,B}/S$.

It is also convenient to define smooth conduction electron spin densities on each of the two sublattices

$$\mathbf{s}^{A,B}(\mathbf{r}) = \frac{1}{2} \sum_{i\sigma\sigma'} \langle c_{i\sigma}^\dagger \boldsymbol{\sigma}_{\sigma\sigma'} c_{i\sigma'} \rangle \frac{2}{\mathcal{A}}, \quad (2.17)$$

where \mathcal{A} is the area of the unit cell (which naturally includes one A and one B site). Thus, the equation of motion (2.16) can be written in continuous approximation as

$$\dot{\mathbf{n}}^A = \mathbf{H}^A \times \mathbf{n}^A + (J\mathcal{A}/\hbar) \mathbf{n}^A \times \mathbf{s}^A, \quad (2.18a)$$

$$\dot{\mathbf{n}}^B = \mathbf{H}^B \times \mathbf{n}^B + (J\mathcal{A}/\hbar) \mathbf{n}^B \times \mathbf{s}^B, \quad (2.18b)$$

where $|\mathbf{n}^{A,B}| = 1$, and the notations $\mathbf{H}^{A,B}$ refer to the effective fields on the sublattices A and B.

Antiferromagnet dynamics is usually formulated as the coupled dynamics of the Néel and magnetization vectors,

$$\boldsymbol{\ell} = (\mathbf{n}^A - \mathbf{n}^B)/2, \quad \mathbf{m} = (\mathbf{n}^A + \mathbf{n}^B)/2, \quad (2.19)$$

that remain mutually perpendicular $\boldsymbol{\ell} \cdot \mathbf{m} = 0$ and yield the constraint $\ell^2 + m^2 = 1$. Naturally, the amplitude of the magnetization vector remain to be small, $m \ll \ell \approx 1$.

For an “isotropic” antiferromagnet, one finds the effective field [Gomonay2014] $\mathbf{H}^A + \mathbf{H}^B = J_{\text{ex}} \mathbf{m}/\hbar + 2\mathbf{H}$, where \mathbf{H} is an external magnetic field in frequency units and J_{ex} is a direct antiferromagnetic exchange energy that is one of the largest energies in the problem. In turn, the combination $\mathbf{H}^A - \mathbf{H}^B$ is proportional to magnetic anisotropy that we choose not to take into account as mentioned above.

Equations (2.18) can, therefore, be rewritten as

$$\begin{aligned} \dot{\boldsymbol{\ell}} &= -\frac{J_{\text{ex}}}{2\hbar} \boldsymbol{\ell} \times \mathbf{m} + \mathbf{H} \times \boldsymbol{\ell} + \frac{J\mathcal{A}}{\hbar} (\boldsymbol{\ell} \times \mathbf{s}_+ + \mathbf{m} \times \mathbf{s}_-), \\ \dot{\mathbf{m}} &= \mathbf{H} \times \mathbf{m} + \frac{J\mathcal{A}}{\hbar} (\mathbf{m} \times \mathbf{s}_+ + \boldsymbol{\ell} \times \mathbf{s}_-), \end{aligned} \quad (2.20)$$

where $\mathbf{s}_{\pm} = (\mathbf{s}_A \pm \mathbf{s}_B)/2$. The right-hand sides of Eqs. (3.5) contain the quantities that can be called generalized torques. Here we are only interested in specific contributions to generalized torques that are induced by the chemical potential difference $\delta\mu = eV_{\text{bias}}$ between left and right leads. Such contributions define four spin-orbit torques

$$\mathbf{T}_{\pm}^{\ell} = (JA/\hbar)\boldsymbol{\ell} \times \delta\mathbf{s}_{\pm}, \quad \mathbf{T}_{\pm}^m = (JA/\hbar)\mathbf{m} \times \delta\mathbf{s}_{\pm}, \quad (2.21)$$

where $\delta\mathbf{s}_{\pm}$ refers to the non-equilibrium spin density contribution that is proportional to $\delta\mu$.

Note that, generally, the average spin \mathbf{s}_i has a non-local functional dependence on the time-dependent classical field \mathbf{S}_j at preceding moments of time and at different lattice sites $j \neq i$. The degree of non-locality is defined by relaxation processes. The quicker the relaxation the more local the functional dependence. In particular, non-dissipative contributions to spin-orbit torques (the so-called field-like contributions) are local in time on the time scales of the order of s-d exchange $\tau_{\text{sd}} = \hbar/\Delta$, where $\Delta = JS$. In contrast, the dissipative contributions (such as anti-damping torques) are defined by transport scattering time τ_{tr} . The latter time scale may be both larger and smaller than τ_{sd} giving rise to different regimes of magnetization dynamics. For the sake of numerical analysis we consider, however, a situation when these two time scales are of the same order.

2.6 SYMMETRY CONSIDERATION

Symmetry properties of spin-orbit torques and conductivity tensor can be understood from a low-energy approximation by projecting the model (2.1) on the states in a vicinity of K points,

$$\mathbf{K} = \frac{4\pi}{3\sqrt{3}a} \begin{pmatrix} 1 \\ 0 \end{pmatrix}, \quad \text{and} \quad \mathbf{K}' = -\mathbf{K}, \quad (2.22)$$

as it is usually done for graphene. In the valley symmetric approximation we obtain the effective model

$$H_0^{\text{eff}} = v\mathbf{p} \cdot \boldsymbol{\Sigma} + \alpha_R [\boldsymbol{\sigma} \times \boldsymbol{\Sigma}]_z - \Delta \boldsymbol{\ell} \cdot \boldsymbol{\sigma} \Sigma_z \Lambda_z, \quad (2.23)$$

where $\boldsymbol{\Sigma}$, Λ , and $\boldsymbol{\sigma}$ are the vectors of Pauli matrices in sublattice, valley and spin space, respectively, and

$$v = \frac{3}{2}ta/\hbar, \quad \alpha_R = \frac{3}{2}\lambda, \quad \Delta = JS. \quad (2.24)$$

Even though the model of Eq. (2.1) is characterized by the point group C_{3v} , the effective low-energy model of Eq. (2.23) has a higher symmetry of the group $C_{\infty v}$.

This is reflected by the fact that the Fermi-surfaces (for energies we are interested in) remain entirely isotropic irrespective of the Néel vector orientation as shown in Fig. 3.1. Moreover, the exact sublattice symmetry of the model, $\Lambda_x H_0^{\text{eff}}[-\ell] \Lambda_x = H_0^{\text{eff}}[\ell]$, ensures vanishing non-equilibrium staggered spin polarization $\delta s_- = 0$ irrespective of both the voltage bias and the Néel vector orientation. This property is indeed confirmed by the numerical analysis.

The spin-orbit coupling term in Eq. (2.23) is proportional to the scalar product $\sigma \cdot [\hat{z} \times v]$, where $v = v\hat{\Sigma}$ is the velocity operator and \hat{z} is the unit vector in z direction. In the presence of electric current I , which, in our model, is always directed along x axis, the velocity operator averages to a non-zero value that is proportional to the current. One can see, therefore, that the second term in Eq. (2.23) can be interpreted as Zeeman coupling to an effective Rashba field $\hat{z} \times I$. Such a field induces non-equilibrium polarization δs_+ in the same way as in ferromagnets.

The symmetry of the point group $C_{\infty v}$ (see also the symmetry analysis in Refs. Duine2012, Garelo2013) suggests that the tensor relation between non-equilibrium polarization δs_+ and the Rashba field $\hat{z} \times I$ can be presented in a vector form as

$$\begin{aligned} \delta s_+ = & A_I(\ell_z^2) \hat{z} \times I + A'_I(\ell_z^2) \ell_{\parallel} \times [\ell_{\parallel} \times [\hat{z} \times I]] \\ & + B_{\perp}(\ell_z^2) \ell_{\perp} \times [\hat{z} \times I] + B_{\parallel}(\ell_z^2) \ell_{\parallel} \times [\hat{z} \times I] \\ & + C(\ell_z^2) \ell_{\parallel} \times [\ell_{\perp} \times [\hat{z} \times I]], \end{aligned} \quad (2.25)$$

where we decompose the Néel vector $\ell = \ell_{\parallel} + \ell_{\perp}$ into in-plane ℓ_{\parallel} and perpendicular-to-the-plane ℓ_{\perp} components. We parameterize $\ell = (\cos \phi \sin \theta, \sin \phi \sin \theta, \cos \theta)^T$, where θ is a polar angle and ϕ is an azimuthal angle. Consequently, we have $\ell_{\parallel} = (\cos \phi \sin \theta, \sin \phi \sin \theta, 0)^T$ and $\ell_{\perp} = (0, 0, \cos \theta)^T$.

The decomposition of Eq. (2.25) is dictated by the symmetry analysis with respect to two transformations: the Néel vector inversion, $\ell \rightarrow -\ell$, and the Néel vector reflection, $\ell_{\perp} \rightarrow -\ell_{\perp}$, with respect to the electron 2D plane.

Since the model (at the Fermi energies we choose) is isotropic with respect to in-plane rotations, these two symmetries are the only ones to characterize different contributions to non-equilibrium spin density.

The first two terms in Eq. (2.25) are even with respect to both the Néel vector inversion and the Néel vector reflection. The last term in Eq. (2.25) is even with respect to the Néel vector inversion but odd with respect to the Néel vector reflection. These terms correspond to torques of the field-like symmetry, i. e. to the torques that are invariant under the time reversal operation.

The second two terms in Eq. (2.25), which are proportional to the coefficients $B_{\parallel, \perp}$, are odd with respect to the Néel vector reflection. The first one of them is odd while the second one is even with respect to the Néel vector reflection.

Figure 2.6: Non-equilibrium spin density δs_+ for the symmetric coupling model of Eqs. (2.1)-(2.6) with $V_d = 0.5 t$ as the function of the Néel-vector orientation for different values of the Fermi energy. Each data point for each direction of the Néel vector corresponds to averaging over 30 impurity configurations. Spin densities are normalized to the scale $\Delta\lambda j / e v t^2$, where $j = I/W$ is the charge current density through the sample. Fluctuations at $\theta = \pi/4$ and $\theta = 3\pi/4$ in the top panel and at $\theta = \pi/2$ in the middle panel are due to diverging mean free path for Fermi energy touching the bottom of the conduction band. The staggered spin density δs_- fluctuates around zero (not-shown). For $E/t = 0$, the spin-density δs_+ also fluctuates around zero as shown in the upper panel.

These terms represent anti-damping spin-orbit torques that change sign under time reversal.

The coefficients in front of different vector forms in Eq. (2.25) must remain invariant with respect to both symmetry transformations, but they may still vary as the function of the symmetry invariant ℓ_z^2 . The coefficients may also depend on ℓ^2 but such dependence is absent within linear response approximation. Indeed, one shall take $\ell^2 = 1$ ($m = 0$) in all coefficients in front of electric current since electric current is regarded as the only possible source of a deviation from the exact antiferromagnetic order.

The exact sublattice symmetry of the symmetric coupling model of Eqs. (2.1)-(2.6) does not only ensure the vanishing staggered polarization $\delta s_- = 0$ but also leads to identically vanishing anti-damping torques $B_{\parallel} = B_{\perp} = 0$ in all possible regimes. This is indeed confirmed by our numerical analysis for the symmetric coupling model as we describe below.

2.7 RESULTS FOR SYMMETRIC MODEL

2.7.1 General

With the help of the kwant package [Groth2014] we compute from Eq. (2.15) the mean spin density response $\delta s / \delta \mu$ on both sublattices for various directions of the Néel vector ℓ and three different Fermi energies. These results, which are presented in Fig. 2.6, have complex dependence on the orientation of the Néel vector. The dependence is, however, much simplified for non-equilibrium spin density response divided by the sample conductance. In other words, we observe that the non-equilibrium spin density has a much simpler form when expressed via the charge current density $j = I/W$ rather than via the bias voltage.

In all regimes considered we find $\delta s_- = 0$ and confirm the decomposition of Eq. (2.25) with $B_{\parallel} = B_{\perp} = 0$. Moreover, we also find that the coefficient $A_I(\ell_z^2) = A_I$ is constant, i.e. independent of the angle θ in all regimes we

Figure 2.7: The results of fitting simulation data for the symmetric coupling model with $L = 2W = 750 \text{ \AA}$ (partly shown in Fig. 2.6) with the ansatz of Eq. (2.28). The data is obtained for $V_d = 0.5 \text{ t}$. The data have been collected for 200 different orientations of the Néel vector for each impurity concentration.

consider. In addition, we find that the non-equilibrium spin density vanishes identically, $\delta s_+ = \delta s_- = 0$ for $E = 0$. This point corresponds to the exact electron-hole symmetry of the model, i. e. for $E = 0$, the number of quasiparticles in the conduction and valence bands are exactly the same.

Despite these general findings we still observe that the results for non-equilibrium spin density are qualitatively different in the metal and half-metal regimes.

2.7.2 Metal regime

The metal regime is characterized by two Fermi surfaces for each of the two valleys. This regime is represented in our simulations by the choice $E = 0.3 \text{ t}$. In this case we also find $A'_I = C = 0$ within our numerical accuracy. Thus, the metal regime in the symmetric model is represented by the only contribution to the non-equilibrium spin-density

$$\delta s_+ = \frac{\Delta\lambda}{2\pi\text{evt}^2} \alpha_I \hat{z} \times \mathbf{j}, \quad (2.26)$$

with a constant dimensionless coefficient α_I . This coefficient retains almost the same value for three different impurity concentrations as shown in the left panel of Fig. 2.7. Thus, the non-equilibrium spin density in the metal regime is simply proportional to the Rashba field. The non-equilibrium spin density of Eq. (2.26) is readily recognized as the inverse spin-galvanic effect of Edelstein [Edelstein1990] that is widely known in ferromagnet materials with Rashba coupling [ManchonPRB2008, GarateSOT2009].

Consequently, the spin orbit torques in the metal regime of the symmetric model are given solely by the isotropic Edelstein effect as

$$\mathbf{T}_+^\ell = \alpha_I \eta \ell \times [\hat{z} \times \mathbf{j}], \quad \mathbf{T}_+^m = \alpha_I \eta \mathbf{m} \times [\hat{z} \times \mathbf{j}], \quad (2.27)$$

where $\eta = J\Delta\lambda/\text{evht}^2$.

This results of Eqs. (2.26), (2.27) are remarkably similar to those found analytically in the metal regime of a Rashba ferromagnet model with white-noise disorder [AdoSOT2017, AdoSTTGD2019]. The latter is also characterized by identically vanishing anti-damping spin-orbit torques and by a completely isotropic field-like torque of the same symmetry. Even though, analytical results have been obtained for a ferromagnet with a weak white-noise disorder, the same drastic

simplification of the spin-orbit torque takes place for a symmetric honeycomb antiferromagnet with rather strong point-like disorder as demonstrated above. Such a simplification is, however, limited to the metal regime.

2.7.3 Half-metal regime

The half-metal regime is represented by the Fermi energy $E = 0.05 t$ that corresponds to the presence of a single Fermi surface in one of the valleys. The conductivity in this regime acquires strong dependence on θ . In particular, for $\ell_z^2 < 1/2$, the system is poorly conducting as one can see already in the second panel of Fig. 2.5. Remarkably, we still find that the coefficient A_I in Eq. (2.25) is entirely independent of θ and anti-damping like torques are vanishing identically, $B_{\parallel,\perp} = 0$. The coefficients A'_I and C are, however, finite and acquire some dependence on ℓ_z^2 .

Thus, our numerical data in half-metal regime corresponds to the spin density

$$\delta \mathbf{s}_+ = \frac{\Delta \lambda}{2\pi e v t^2} \left(a_I \hat{\mathbf{z}} \times \mathbf{j} + a'_I(\ell_z^2) \ell_{\parallel} \times [\ell_{\parallel} \times [\hat{\mathbf{z}} \times \mathbf{j}]] + c(\ell_z^2) \ell_{\parallel} \times [\ell_{\perp} \times [\hat{\mathbf{z}} \times \mathbf{j}]] \right), \quad (2.28)$$

where we also introduced the dimensionless functions $a'_I(\ell_z^2)$ and $c(\ell_z^2)$ that are shown in the middle and in the right panel of Fig. 2.7 for different impurity concentrations.

The last two terms in Eq. (2.28) represent high-harmonics field-like torques that are finite only in the half-metal regime. On symmetry grounds one should generally expect the field-like torques to be largely insensitive to disorder. Even though, the disorder dependence of a_I and a'_I coefficients is indeed negligible, the one of the function $c(\ell_z^2)$ is still rather strong for $\ell_z^2 < 1/2$. One should, however, remember that the coefficient c is standing in front of the vector form that is vanishing for both $\ell_z = 0$ and $\ell_z = \pm 1$, so the fit accuracy near these points is poor. Moreover, the case of almost in-plane Néel vector, $\ell_z^2 \ll 1/2$, corresponds to the poorly conducting sample whose conductance is dominated by the variable range hopping processes due to strong disorder. Thus, we attribute this seemingly strong dependence of c on disorder concentration to the mechanism of conduction. Still, the value of c is found to be about 5 times larger than that of a_I and about 10 times larger than that of a'_I , which makes the high-harmonic c -torque relevant in the half-metal regime. We note that the non-equilibrium spin density, which is proportional to $c(\ell_z^2)$, is directed perpendicular to the electron plane.

Overall, the half-metal regime is characterized by the torques

$$\begin{aligned} \mathbf{T}_+^\ell = \eta \Big(& \alpha_I \ell \times [\hat{\mathbf{z}} \times \mathbf{j}] + \alpha'_I(\ell_z^2) \ell \times \left[\ell_{\parallel} \times \left[\ell_{\parallel} \times [\hat{\mathbf{z}} \times \mathbf{j}] \right] \right. \\ & \left. + c(\ell_z^2) \ell \times \left[\ell_{\parallel} \times [\ell_{\perp} \times [\hat{\mathbf{z}} \times \mathbf{j}]] \right] \right), \end{aligned} \quad (2.29a)$$

$$\begin{aligned} \mathbf{T}_+^m = \eta \Big(& \alpha_I \mathbf{m} \times [\hat{\mathbf{z}} \times \mathbf{j}] + \alpha'_I(\ell_z^2) \mathbf{m} \times \left[\ell_{\parallel} \times \left[\ell_{\parallel} \times [\hat{\mathbf{z}} \times \mathbf{j}] \right] \right. \\ & \left. + c(\ell_z^2) \mathbf{m} \times \left[\ell_{\parallel} \times [\ell_{\perp} \times [\hat{\mathbf{z}} \times \mathbf{j}]] \right] \right), \end{aligned} \quad (2.29b)$$

where $\eta = J\Delta\lambda/\text{evht}^2$ is the same as in Eq. (2.27).

Note, that the function $\alpha'_I(\ell_z^2)$ in Eq. (2.29a) for \mathbf{T}_+^ℓ can be absorbed into the redefinition of the coefficients α_I and c . Indeed, with the help of a straightforward vector algebra one can re-write Eq. (2.29a) as

$$\mathbf{T}_+^\ell = \eta \left(\tilde{\alpha}_I(\ell_z^2) \ell \times [\hat{\mathbf{z}} \times \mathbf{j}] + \tilde{c}(\ell_z^2) \ell \times \left[\ell_{\parallel} \times [\ell_{\perp} \times [\hat{\mathbf{z}} \times \mathbf{j}]] \right] \right), \quad (2.30)$$

where we introduced

$$\tilde{\alpha}_I = \alpha_I - (1 - \ell_z^2) \alpha'_I, \quad \tilde{c} = c - \alpha'_I. \quad (2.31)$$

Thus, the modified coefficient $\tilde{\alpha}_I$ acquires a weak dependence on ℓ_z^2 due to a finite, though small, α'_I contribution in the half-metal regime.

To conclude this section it is worth mentioning that half-metal antiferromagnets are not entirely hypothetical. There have been several proposals in the past (see Refs. deGroot1995, Gong2018 to name a few) and there has been also a recent material $\text{Mn}_2\text{Ru}_x\text{Ga}$ that is recognized as a half-metal antiferromagnet [Kurt2014, Coey2016].

2.8 ASYMMETRIC COUPLING MODEL

Relative simplicity of the results of Eqs. (2.27,2.29) for the symmetric coupling model of Eqs. (2.1)-(2.6) prompted us to look at a model with ultimately asymmetric s-d exchange,

$$H_{\text{sd}} = -J \sum_{i \in A} \sum_{\sigma\sigma'} \sigma_{\sigma\sigma'} S_i^A \cdot c_{i\sigma}^\dagger c_{i\sigma'}, \quad (2.32)$$

that is represented by s-d coupling on A sublattice only. Such a coupling obviously violates the sublattice symmetry and may, in principle, lead to the appearance of non-equilibrium staggered polarization and to anti-damping like spin-orbit torques that are absent in the symmetric coupling model.

It is worth mentioning that the asymmetric model is unlikely to represent an antiferromagnet. Since conduction electron spins contribute to polarization

Figure 2.8: Band structure for the asymmetric model. Dotted horizontal lines correspond to $E/t = 0, 0.1$, and 0.3 .

only on a single sublattice, the model is much more likely to correspond to a ferrimagnet or a ferromagnet. Rare-earth/transition metal ferrimagnets (such as FeCoGd) at a compensation point seem to be the most obvious examples [Hoffman2018]. The conduction electrons in these compounds couple mostly with localized d-orbitals rather than with f-orbitals and give rise to an asymmetric exchange coupling that can be mimicked by Eq. (2.32).

In order to compute non-equilibrium spin-densities we repeat the analysis of the previous sections for the coupling of Eq. (2.32) that we refer to below as the asymmetric model. The band-structure of the asymmetric model is illustrated in Fig. 2.8. Similarly to the symmetric model we distinguish metal and half-metal regimes that are represented now by $E = 0.3 t$ and $E = 0.1 t$, correspondingly.

The metal regime is characterized by two Fermi surfaces per valley, while the half-metal regime is characterized by a single Fermi surface per valley. The Fermi surfaces are illustrated in Fig. 2.9 for $\theta = -\phi = \pi/4$, where θ and ϕ are now the polar and azimuthal angles of the unit vector $\mathbf{n}^A = (\cos \phi \sin \theta, \sin \phi \sin \theta, \cos \theta)^\top$, correspondingly.

For numerical simulations we choose $\Delta = JS = 0.1 t$, $\lambda = 0.05 t$, and $V_d = 0.5 t$ as for the symmetric model.

Similarly to Eq. (2.23) the low energy sector of the asymmetric model is represented by the following effective Hamiltonian

$$H_0^{\text{as}} = v \mathbf{p} \cdot \boldsymbol{\Sigma} + \alpha_R [\boldsymbol{\sigma} \times \boldsymbol{\Sigma}]_z - \frac{\Delta}{2} \mathbf{n}^A \cdot \boldsymbol{\sigma} (1 + \Sigma_z \Lambda_z), \quad (2.33)$$

that clearly lacks the sublattice symmetry. Interestingly, we observe from numerical simulations that the staggered non-equilibrium polarization δs_- is still vanishing in the metal regime, while it becomes finite in the half-metal regime. It has to be noted, however, that the separation to staggered and non-staggered polarization is largely irrelevant for the asymmetric model, since the latter is characterized by the only vector torque

$$\mathbf{T}^A = \frac{J_A}{\hbar} \mathbf{n}^A \times \delta \mathbf{s}^A = \frac{J_A}{\hbar} (\boldsymbol{\ell} + \mathbf{m}) \times (\delta \mathbf{s}_+ + \delta \mathbf{s}_-), \quad (2.34)$$

that is defined exclusively by the spin density on the sublattice A.

Indeed, for an “isotropic” antiferromagnet we find, in complete analogy with Eqs. (3.5), the equations of motion

$$\dot{\boldsymbol{\ell}} = -(J_{\text{ex}}/2\hbar) \boldsymbol{\ell} \times \mathbf{m} + \mathbf{H} \times \boldsymbol{\ell} + \mathbf{T}^A, \quad (2.35a)$$

$$\dot{\mathbf{m}} = \mathbf{H} \times \mathbf{m} + \mathbf{T}^A, \quad (2.35b)$$

Figure 2.9: The Fermi surfaces for the asymmetric model for the metal regime $E = 0.3 t$ (right panel) and the half-metal regime $E = 0.1 t$ (left panel). The Fermi surfaces are not round due to tridiagonal wrapping originating in C_{3v} point-group symmetry of the crystal and due to in-plane component \mathbf{n}_{\parallel}^A that affects the spectrum. The plots correspond to the choice $\theta = -\phi = \pi/4$. The momentum \mathbf{k} is measured with respect to \mathbf{K} point (solid lines) and \mathbf{K}' point (dashed lines).

which depend only on the spin-orbit torque T^A .

We would like to remind that the equations of motion of Eq. (3.8) are essentially incomplete since we do not investigate Gilbert-damping terms and we do not take into account anisotropy of antiferromagnet (as well as Dzyaloshinskii-Moriya interaction terms). The missing terms are essential if one wants to understand the magnetization dynamics, while they cannot alter the spin-orbit torque terms that we compute.

As one can readily see from Fig. 2.9, the Fermi surfaces in the asymmetric model are not entirely round and reveal some tri-diagonal wrapping even for energies that are close to zero, $E \ll t$. The Fermi surfaces are also shifted with respect to the points \mathbf{K} and \mathbf{K}' and deformed depending on the azimuthal angle ϕ characterizing in-plane orientation of the vector \mathbf{n}^A . We find, however, that despite these effects the non-equilibrium spin-density δs^A can be very well decomposed using the symmetry analysis of the group $C_{\infty v}$ in analogy to Eq. (2.25) for the symmetric coupling model.

To do that we represent the vector $\mathbf{n}^A = \mathbf{n}_{\parallel}^A + \mathbf{n}_{\perp}^A$ as the sum of in-plane and perpendicular-to-the-plane components and decompose the numerical data with respect to the transformations: $\mathbf{n}_{\perp}^A \rightarrow -\mathbf{n}_{\perp}^A$ and $\mathbf{n}_{\parallel}^A \rightarrow -\mathbf{n}_{\parallel}^A$. As the result, the non-equilibrium spin density (as the function of the vector components) is readily decomposed into the sum of four contributions,

$$\delta s^A[\mathbf{n}_{\perp}^A, \mathbf{n}_{\parallel}^A] = \delta s_{++} + \delta s_{+-} + \delta s_{-+} + \delta s_{--}, \quad (2.36)$$

which are expressed as

$$\begin{aligned} \delta s_{\zeta\kappa} = & \frac{1}{4} \left(\delta s^A[\mathbf{n}_{\perp}^A, \mathbf{n}_{\parallel}^A] + \zeta \delta s^A[-\mathbf{n}_{\perp}^A, \mathbf{n}_{\parallel}^A] \right. \\ & \left. + \kappa \delta s^A[\mathbf{n}_{\perp}^A, -\mathbf{n}_{\parallel}^A] + \zeta\kappa \delta s^A[-\mathbf{n}_{\perp}^A, -\mathbf{n}_{\parallel}^A] \right), \end{aligned} \quad (2.37)$$

where ζ and κ take on the values ± 1 .

The bare results for non-equilibrium spin density δs^A (with a subtracted background component along \mathbf{n}^A) and the results for the contributions $\delta s_{\zeta\kappa}$ are shown in Fig. 2.10 for the metal regime, $E = 0.3 t$. Similar results are obtained for the half-metal regime, $E = 0.1 t$.

Figure 2.10: Top panels show non-equilibrium spin density, δs^A , for the asymmetric coupling model with subtracted background component along \mathbf{n}^A in the units of $\Delta\lambda j/\text{evt}^2$. The other panels represent the results of the spin-density decomposition of Eq. (2.36). The results presented correspond to the ansatz of Eq. (2.38). The data for density plots have been collected for 200 different orientations of the Néel vector for each impurity concentration. Each data point corresponds to averaging over at least 80 impurity configurations.

Figure 2.11: Numerical results for the asymmetric coupling model that are expressed in the form of the angle dependent coefficients a_I , b_\perp , b_\parallel , and c that define the spin-orbit torque \mathbf{T}^A in Eq. (2.39). The data is obtained by fitting the density data (partially represented in Fig. 2.10) using the a of Eq. 2.38.

We find that our numerical results for the non-equilibrium spin density δs^A (with subtracted background along \mathbf{n}^A that does not enter the torque \mathbf{T}^A) are perfectly decomposed as a sum of five different vector forms in both metal and half-metal regimes,

$$\begin{aligned} \delta s^A = & A_I(n_z^2) \hat{\mathbf{z}} \times \mathbf{I} + A'_I(n_z^2) \mathbf{n}_\parallel^A \times [\mathbf{n}_\parallel^A \times [\hat{\mathbf{z}} \times \mathbf{I}]] \\ & + B_\perp(n_z^2) \mathbf{n}_\perp^A \times [\hat{\mathbf{z}} \times \mathbf{I}] + B_\parallel(n_z^2) \mathbf{n}_\parallel^A \times [\hat{\mathbf{z}} \times \mathbf{I}] \\ & + C(n_z^2) \mathbf{n}_\parallel^A \times [\mathbf{n}_\perp^A \times [\hat{\mathbf{z}} \times \mathbf{I}]], \end{aligned} \quad (2.38)$$

where all coefficients are generally even functions of the component $n_z = n_z^A = \cos \theta$. Note that the first two vector forms are of the same symmetry with respect to both reflections $\mathbf{n}_\perp^A \rightarrow -\mathbf{n}_\perp^A$ and $\mathbf{n}_\parallel^A \rightarrow -\mathbf{n}_\parallel^A$.

Remarkably, our numerical data again corresponds to a constant coefficient $A_I(n_z^2) = A_I$ in all regimes considered as it was also the case for the symmetric model.

The spin orbit torque \mathbf{T}^A , which is obtained by substituting the result of Eq. (2.38) to Eq. (2.34), can be represented as the sum of only four vector forms

$$\begin{aligned} \mathbf{T}^A = \eta \Big(& a_I(n_z^2) \mathbf{n}^A \times [\hat{\mathbf{z}} \times \mathbf{j}] \\ & + b_\perp(n_z^2) \mathbf{n}^A \times [\mathbf{n}_\perp^A \times [\hat{\mathbf{z}} \times \mathbf{j}]] \\ & + b_\parallel(n_z^2) \mathbf{n}^A \times [\mathbf{n}_\parallel^A \times [\hat{\mathbf{z}} \times \mathbf{j}]] \\ & + c(n_z^2) \mathbf{n}^A \times [\mathbf{n}_\parallel^A \times [\mathbf{n}_\perp^A \times [\hat{\mathbf{z}} \times \mathbf{j}]]] \Big), \end{aligned} \quad (2.39)$$

where we again introduce $\eta = J\mathcal{A}\Delta\lambda/\text{evht}^2$, $\mathbf{j} = \mathbf{I}/W$ and the dimensionless coefficients a_I , b_\perp , b_\parallel , and c that all appear to be non-trivial functions of $n_z^2 =$

$\cos^2 \theta$ as shown in Fig. 2.11. Note that the function $A'_1(n_z^2)$ in Eq. (2.38) for spin density contributes to both a_\perp and c coefficients in Eq. (2.39) in the direct analogy to Eqs. (2.30) and (2.31).

Thus, the spin-orbit torque T^A is parameterized by 4 dimensionless functions. These functions are shown in Fig. 2.11 illustrating the main result of our numerical simulations for the asymmetric coupling model. In sharp contrast to the symmetric model we observe that the anti-damping torques are no longer vanishing. We also find that $b_\perp(n_z^2) \approx b_\parallel(n_z^2)$ in the half-metal regime. The major field-like torque $\mathbf{n}^A \times [\hat{\mathbf{z}} \times \mathbf{j}]$, which originates in the Edelstein effect, acquires a weak dependence on θ due to the impact of the coefficient $A'_1(n_z^2)$.

As it is expected we observe that anti-damping torques, which are proportional to $b_{\perp,\parallel}$, depend strongly on disorder concentration, while the field-like torques do not. Moreover, while anti-damping torques are suppressed by disorder in the metal regime, the opposite is true in the half-metal regime.

Similarly to the symmetric model, the field-like torques are smaller in the metal regime than they are in half-metal regime. One can speculate, however, that anti-damping-like torques play a leading role in the metal regime of the asymmetric coupling model for sufficiently clean samples. We also see that anti-damping torques reveal rather strong anisotropy. In the metal regime they take on maximal values for in-plane orientations of the vector \mathbf{n}^A .

It is also worth stressing that our results for asymmetric coupling model are the same for both ferromagnetic and antiferromagnetic order, since the spin-orbit torques are insensitive to the direction of the field \mathbf{n}^B .

As have been already mentioned one can expect the asymmetric model to capture also the physics of layered ferrimagnets such as GdFeCo or Pt/GdFeCo [Hoffman2018, KimFERRISOT018]. The magnetization switching by means of spin-orbit torques in these materials has recently become a subject of intense studies [Roschewsky2016, Roschewsky2017, KimFERRISOT018]. In particular, the contribution from both field-like and anti-damping-like torques have been identified in GdFeCo films with perpendicular magnetocrystalline anisotropy in both transition-metal and rare-earth-metal rich configurations [Roschewsky2016, Roschewsky2017]. These experimental results are, at least, qualitatively in line with our findings.

2.9 CONCLUSIONS

Motivated by recent experiments on the Néel vector switching we investigate microscopically the spin-orbit torques in an s-d-like model of a two-dimensional honeycomb antiferromagnet with Rashba spin-orbit coupling. We investigated the model with preserved and broken sublattice symmetry and distinguished metal and half-metal regimes for each of the model. Spin-orbit interaction in

combination with on-site disorder potential and local exchange coupling between conduction and localized spins have been responsible for a microscopic mechanism of the angular momentum relaxation. We find identically vanishing anti-damping and Néel spin-orbit torques in the symmetric model in all regimes considered. As the result, the metal regime of the symmetric model is characterized by a particularly simple isotropic field-like spin-orbit torque, while the half-metal regime is characterized by anisotropic spin-orbit torques of the field-like symmetry. Finite and anisotropic anti-damping torques, that crucially depend on disorder strength, are found in both metal and half-metal regimes of the asymmetric model. We also find non-equilibrium staggered polarization in the half-metal regime of the asymmetric model. This formally leads to a finite value of the Néel spin-orbit torque, which is, however, not a quantity of interest in that model. Overall, our results reveal the importance of two-dimensional electron momentum confinement for spin-orbit torque anisotropy. Largest values of spin-orbit torques are also associated with the half-metal regimes of conduction in both models.

GILBERT DAMPING IN RASHBA HONEYCOMB
ANTIFERROMAGNETS

Giant Gilbert damping anisotropy is identified as a signature of strong Rashba spin-orbit coupling in a two-dimensional antiferromagnet on a honeycomb lattice. The phenomenon originates in spin-orbit induced splitting of conduction electron subbands that strongly suppresses certain spin-flip processes. As a result, the spin-orbit interaction is shown to support an undamped non-equilibrium dynamical mode that corresponds to an ultrafast in-plane Néel vector precession and a constant perpendicular-to-the-plane magnetization. The phenomenon is illustrated on the basis of a two dimensional s - d like model. Spin-orbit torques and conductivity are also computed microscopically for this model. Unlike Gilbert damping these quantities are shown to reveal only a weak anisotropy that is limited to the semiconductor regime corresponding to the Fermi energy staying in a close vicinity of antiferromagnetic gap.

3.1 INTRODUCTION

A gapless character of the spin-wave spectrum in isotropic Heisenberg magnets in two dimensions results in the homogeneity of magnetic ordering being destroyed by thermal fluctuations at any finite temperatures. In contrast, in van der Waals magnets, characterized by intrinsic magnetocrystalline anisotropy that stems from spin-orbit coupling [Lado2017], an ordered magnetic state can be retained down to a monolayer limit. Two-dimensional (2D) van der Waals magnets are currently experiencing a revived attention [Gong2017, Herrero2017, Burch2018, Tokmachev2018, Gong2019, Novoselov2019, Cortie2019] driven by the prospects of gateable magnetism [Huang2018, Shengwei2018, Wang2018, Deng2018], a continuing search for Kitaev materials [Nagler2019, Gordon2019] and Majorana fermions [Livanas2019], topologically driven phenomena [Mokrousov2019] as well as various applications [Herrero2017, Burch2018, Novoselov2019]. The trade-off between quantum confinement, nontrivial topology and long-range magnetic correlations determines their unique magnetoelectronic properties, in particular a tunable tunneling conductance [Wang2018a] and magnetoresistance [Song2018, Klein2018, Kim2018] depending on the number of layers in the sample, as well as long-distance magnon transport [Xing2019].

Ferromagnetic thin films have already entered commercial use in hard drives, magnetic field and rotation angle sensors and in similar devices [Parkin2003, Jogschies2015, Novoselov2019], while keeping high promises for technologically competitive ultrafast memory elements [Lau2016] and neuromorphic chips [Fukami2016]. Moreover, it has recently been suggested that current technology may have a lot to gain from antiferromagnet (AFM) materials. Indeed, manipulating AFM domains does not induce stray fields and has no fundamental speed limitations up to THz frequencies [Jungwirth2016AFMreview]. Despite their ubiquitousness, AFM materials have, however, avoided much attention from technology due to an apparent lack of control over the AFM order parameter – the Néel vector. Switching the Néel vector orientation by short electric pulses has been put forward only recently as the basis for AFM spintronics [MacDonald2011, Gomonay2014, Zelezny2014]. The proposed phenomenon has been soon observed in non-centrosymmetric crystals such as CuMnAs [Wadley2016, Fina2016, Zelezny2018, Saidl2017] and Mn₂Au [Barthem2013, Jordan2015, Bhattacharjee2018]. It should be noted that in most cases AFMs are characterized by insulating type behavior [Pandey2017], limiting the range of their potential applications, e.g., for spin injection [Tshitoyan2015]. Interestingly, antiferromagnetic Mn₂Au possesses a typical metal properties, inheriting strong spin-orbit coupling and high conductivity, and is characterized by collective modes excitations in THz range [Bhattacharjee2018].

Figure 3.1: A model of Rashba honeycomb antiferromagnet with two sublattices, A and B, and on-site exchange interaction between localized momenta and conduction electrons (see Eq. 3.1). The large blue arrow represents the Néel vector vector, \mathbf{n} , that is in general, characterized by non-vanishing in-plane, \mathbf{n}_{\parallel} , and perpendicular-to-the-plane, \mathbf{n}_{\perp} , components. We refer to a specific coordinate system with \hat{x} axis chosen to be in the direction of \mathbf{n}_{\parallel} .

Despite a lack of clarity concerning the microscopic mechanisms of the Néel vector switching, these experiments have been widely regarded as a breakthrough in the emerging field of THz spintronics [Bhattacharjee2018, Gomonay2016AFM, Olejnik2018, Jungwirth2018, Wadley2016, Jungwirth2016AFMreview, Baltz2018, Jungwirth2018, Hoffman2018]. It has been suggested that current-induced Néel vector dynamics in an AFM is driven primarily by the so-called Néel spin-orbit torques [Brataas2012, Hals2013, Zelezny2014, 2014MokrousovSOT, Ghosh2017, SmejkalAFM_2017, Zelezny2018, Zhou2018, Manchon2018, Moriyama2018, Li2019, Chen2019, Zhou2019, Zhou2019a, Bodnar2018]. The Néel spin-orbit torque originates in a non-equilibrium staggered polarization of conduction electrons on AFM sublattices [Zelezny2014, SmejkalAFM_2017, Zelezny2018, Manchon2018]. Characteristic magnitude of the non-equilibrium staggered polarization and its relevance for the experiments with CuMnAs and Mn₂Au remain, however, debated.

The Néel vector dynamics in an AFM is also strongly affected by an interplay between different types of Gilbert dampings. Unlike in a simple single-domain ferromagnet with a single sublattice, the Gilbert damping in an AFM is generally different on different sublattices and includes spin pumping from one sublattice to another. A proper understanding of Gilbert damping is of key importance for addressing not only the mechanism of spin pumping but also domain wall motion, magnon lifetime, AFM resonance width and many other related phenomena [PhysRevMaterials.1.061401, Kamra2018, Mahfouzi2018a, Yuan_2019, Hals2011]. It is also worth noting that spin pumping between two thin ferromagnetic layers with antiparallel magnetic orientations share many similarities with Gilbert damping in a bipartite AFM [Heinrich2003, Tserkovnyak2005].

A conduction electron mechanism for Gilbert damping in collinear ferromagnet requires some spin-orbit interaction to be present. It is, therefore, commonly assumed that spin-orbit interaction of electrons naturally enhances the Gilbert damping. Contrary to this intuition, we show that Rashba spin-orbit coupling does generally suppress one of the Gilbert damping coefficients and leads to the appearance of undamped non-equilibrium Néel vector precession modes in the AFM.

Spin dynamics in a bipartite AFM is described in terms of two mutually orthogonal vector fields, namely the vector $\mathbf{n}(t)$ that is proportional to the Néel vector

(difference between sublattice moments) and the vector $\mathbf{m}(t)$ that is proportional to the net magnetization (sum of sublattice moments) of a sample. Even though the AFM ground state corresponds to $\mathbf{m} = 0$, it is widely understood that no Néel dynamics is possible without formation of a small but finite nonequilibrium magnetization \mathbf{m} . It appears, however, that Gilbert damping terms associated with the time dynamics of $\mathbf{m}(t)$ and $\mathbf{n}(t)$ are essentially different from a microscopic point of view.

Indeed, the Gilbert damping that is proportional to $\partial_t \mathbf{n}$ is characterized by a coefficient α_n , which is vanishing in the absence of spin-orbit interaction, much like it is the case in the ferromagnets. This behavior can be traced back to a spin-rotational symmetry of the collinear AFM. Indeed, the absolute value of \mathbf{n} is conserved up to the order m^2 . Thus, the dynamics of the Néel vector is essentially a rotation that does not change the conduction electron spectrum as far as the spin-rotation invariance is present. Breaking the spin-rotation symmetry by spin-orbit interaction induces, therefore, a finite α_n , which is quadratic with respect to spin-orbit interaction strength.

In contrast, the Gilbert damping that is proportional to $\partial_t \mathbf{m}$ originates directly in the conduction electron scattering even in the absence of any spin-orbit interaction. The strength of the damping in a simple symmetric AFM is characterized by a coefficient α_m , which is typically much larger than α_n . As a rule, the spin-orbit interaction tends to suppress the coefficient α_m by restricting the ways in which electrons can damp their magnetic moments. The condition $\alpha_m \gg \alpha_n$ has been indeed well documented in a metallic AFM [**PhysRevMaterials.1.061401, Mahfouzi2018a**].

In this paper, we uncover the microscopic mechanism of strong and anisotropic Gilbert damping suppression due to the influence of spin-orbit interaction in a 2D AFM model on a honeycomb lattice.

Below we focus mainly on the AFM in the regime of good metallic behavior, such that the Fermi energy of electrons exceeds by order of magnitude that of an effective *s-d* exchange coupling between electron spins and localized AFM magnetic momenta. In this case, the transition to the highly anisotropic regime takes place provided the characteristic spin-orbit energy λ exceeds the scale \hbar/τ , where τ is the electron scattering time. Alternatively, one may think of characteristic spin-orbit length becoming smaller than the mean free path of conduction electrons. We show here that the splitting of 2D Fermi surfaces by spin-orbit interaction leads to a dramatic suppression of electron spin flips in certain directions. This results in a strong anisotropy of both Gilbert damping tensors $\hat{\alpha}_n$ and $\hat{\alpha}_m$, that get some of their principal components vanishing. This extreme anisotropy in the damping leads to essentially undamped Néel vector dynamics for certain nonequilibrium modes.

In particular, we identify a specific undamped mode that corresponds to perpendicular-to-the-plane magnetization $\mathbf{m} \propto \hat{\mathbf{z}}$ and in-plane Néel vector $\mathbf{n}(t) \perp \hat{\mathbf{z}}$. The Néel vector corresponding to the mode has a precession around \mathbf{m} with the frequency $J_{\text{ex}}m/\hbar$, where J_{ex} is the value of the isotropic AFM exchange.

The presence of the undamped mode identified here, illustrates how lowering the symmetry of the electronic bath (by spin-orbit interaction) may induce a conservation law in the localized spin subsystem. Based on this microscopic mechanism we provide qualitative arguments in favor of a generality of the giant Gilbert damping anisotropy in a 2D metallic AFM with spin-orbit coupling. Even though the undamped mode cannot be associated with a single spin-wave or a magnon, its presence has a strong impact on the nonequilibrium Néel vector dynamics in 2D Rashba AFMs.

Apart from the Gilbert damping our results extend to cover conductivity and spin-orbit torques in the Rashba honeycomb AFM model. We also demonstrate how weak anisotropy of all these quantities emerge with Fermi energies approaching the AFM band gap.

3.2 PHENOMENOLOGY OF AFM DYNAMICS

In this paper, we choose to describe the AFM with a classical Heisenberg model for localized spins $\mathbf{S}^X = S\mathbf{n}^X$ on two sublattices $X = A, B$. The spins have the same modulus S and antiparallel directions $\mathbf{n}^A = -\mathbf{n}^B$ in the ground state. The AFM Heisenberg model is coupled to an effective tight-binding model of conduction electrons (see Appendix 3.9) by means of exchange interaction,

$$H_{\text{sd}} = -J \sum_i \sum_{\sigma\sigma'} \mathbf{S}_i \cdot \boldsymbol{\sigma}_{\sigma\sigma'} c_{i\sigma}^\dagger c_{i\sigma'} \quad (3.1)$$

where J stands for an s-d-like exchange energy that is the same on A and B sublattices, the operators $c_{i\sigma}^\dagger$ ($c_{i\sigma}$) are the standard creation (annihilation) operators for an electron on the lattice site i with the spin index σ , and the notation $\boldsymbol{\sigma} = (\sigma_x, \sigma_y, \sigma_z)$ represents the three-dimensional vector of Pauli matrices.

The real-time dynamics of AFM is, then, defined by two coupled differential equations (Landau-Lifshitz-Gilbert equations) on the unit vectors \mathbf{n}^A and \mathbf{n}^B ,

$$\dot{\mathbf{n}}^A = \mathbf{H}^A \times \mathbf{n}^A + (JA/\hbar) \mathbf{n}^A \times \mathbf{s}^A, \quad (3.2a)$$

$$\dot{\mathbf{n}}^B = \mathbf{H}^B \times \mathbf{n}^B + (JA/\hbar) \mathbf{n}^B \times \mathbf{s}^B, \quad (3.2b)$$

where dot stands for the time derivative, \mathbf{s}^X is the spin density of conduction electrons on the sublattice X ,

$$\mathbf{s}^{A,B}(\mathbf{r}) = \frac{1}{2} \sum_{i\sigma\sigma'} \langle c_{i\sigma}^\dagger \boldsymbol{\sigma}_{\sigma\sigma'} c_{i\sigma'} \rangle \frac{2}{\mathcal{A}}, \quad (3.3)$$

Figure 3.2: Electronic band structure of the honeycomb AFM model of Eq. (3.9) for different orientations of the Néel vector ($n_z = \cos \theta$). Two-dimensional momenta \mathbf{p} are measured with respect to the wave-vectors \mathbf{K} and \mathbf{K}' that specify two nonequivalent valleys. Deviation of the Néel vector from the perpendicular-to-the plane configuration ($\theta = 0$) lifts the valley degeneracy. We restrict our analysis to the metallic regime with Fermi energies corresponding to two Fermi surfaces per valley (an example is shown by a black dotted line). The energy scale Δ characterizes the strength of s-d exchange interaction.

and \mathcal{A} is the area of the unit cell in the AFM. The notations $\mathbf{H}^{A,B}$ refer to effective fields on the sublattices A and B that are defined by the Heisenberg model.

For an isotropic antiferromagnet, one finds an effective field [Gomonay2014] $\mathbf{H}^A + \mathbf{H}^B = J_{\text{ex}} \mathbf{m} / \hbar + 2\mathbf{H}$, where \mathbf{H} is an external magnetic field in frequency units and J_{ex} is a direct antiferromagnetic exchange energy that is one of the largest energies in the problem. In turn, the combination $\mathbf{H}^A - \mathbf{H}^B$ is proportional to magnetic anisotropy that we do not specify in this paper.

Magnetization dynamics in AFM is conveniently formulated in terms of the Néel and magnetization vectors,

$$\mathbf{n} = (\mathbf{n}^A - \mathbf{n}^B) / 2, \quad \mathbf{m} = (\mathbf{n}^A + \mathbf{n}^B) / 2, \quad (3.4)$$

that remain mutually perpendicular $\mathbf{n} \cdot \mathbf{m} = 0$ and yield the constraint $n^2 + m^2 = 1$. The dynamics necessarily induces a finite nonequilibrium magnetization vector \mathbf{m} , while the condition $m \ll 1$ remains to be fulfilled.

From Eqs. (3.2) we obtain

$$\dot{\mathbf{n}} = -\Omega \mathbf{n} \times \mathbf{m} + \mathbf{H} \times \mathbf{n} + \mathbf{n} \times \mathbf{s}^+ + \mathbf{m} \times \mathbf{s}^-, \quad (3.5a)$$

$$\dot{\mathbf{m}} = \mathbf{H} \times \mathbf{m} + \mathbf{m} \times \mathbf{s}^+ + \mathbf{n} \times \mathbf{s}^-, \quad (3.5b)$$

where $\Omega = 2J_{\text{ex}}S/\hbar$ and $\mathbf{s}^\pm = J\mathcal{A}(\mathbf{s}^A \pm \mathbf{s}^B)/2\hbar$. In Eqs. (3.5) we have deliberately skipped terms that are induced by anisotropy of AFM exchange since the latter depend on particularities of the AFM Heisenberg model that we do not discuss here.

The vector \mathbf{s}^+ is proportional to average polarization of conduction electrons, while the vector \mathbf{s}^- is proportional to the staggered polarization. The quantities $\mathbf{s}^\pm = \mathbf{s}_0^\pm + \delta\mathbf{s}^\pm$ contain equilibrium contributions \mathbf{s}_0^\pm that characterize various interactions induced by conduction electrons. These contributions do renormalize the parameters of the AFM Heisenberg model and are not the subject of the present paper.

The nonequilibrium contributions $\delta\mathbf{s}^\pm$ originate from various forces applied to conduction electrons. One natural example is the electric field that not only

induces an electric current in the sample but also contributes to δs^\pm . The electric field can be further related to electric current by the resistivity tensor. The response of spin densities to electric current defines the so-called spin-orbit torques in Eqs. (3.5) that we also compute.

Similarly, the response of δs^\pm to the time derivatives \dot{n} and \dot{m} describe various types of Gilbert damping induced by conduction electrons. Quite generally, such a response can be written in the form of a tensor

$$\begin{pmatrix} \delta s^+ \\ \delta s^- \end{pmatrix} = \begin{pmatrix} \hat{\alpha}_m & \hat{\alpha}_{mn} \\ \hat{\alpha}_{nm} & \hat{\alpha}_n \end{pmatrix} \begin{pmatrix} \dot{m} \\ \dot{n} \end{pmatrix}, \quad (3.6)$$

where all tensor components may themselves depend on the vectors n and m .

Gilbert dampings, in their original meaning, correspond to the contributions to δs^\pm that are symmetric under the time reversion. The terms that change sign should, more appropriately, be referred to as effective spin renormalizations. Both types of terms are, however, obtained from the microscopic analysis of the Gilbert damping tensors in Eq. (3.6) similarly to the case of ferromagnets [AdoSTTGD2019].

Time reversion, mentioned above, applies exclusively to the Heisenberg model, while keeping the tight-binding model (a bath) non-reversed. In other words we do not reverse the electron scattering time τ . Such a definition helps to identify the dissipative (even with respect to the time reversion) contributions to δs^\pm that describe Gilbert dampings. These contributions must, however, change sign under the transformation $\tau \rightarrow -\tau$, because spin densities s^\pm are always odd with respect to complete time reversion (the one which also includes that of the electron bath). We will see below, indeed, that all Gilbert dampings are proportional to the scattering time τ in the same way as the longitudinal conductivity does.

Before we proceed with the microscopic analysis of δs^\pm for a particular model, it is instructive to draw some general consequences for Eqs. (3.5) based on symmetry arguments in the case of collinear AFM with sublattice symmetry and spin-rotational invariance (i. e. for vanishing spin-orbit interaction).

Assuming that deviations from the AFM ground state remain small we shall limit ourselves to the linear order in m in Eq. (3.7a) and to the quadratic order in m in Eq. (3.7b). Thus, we shall retain terms up to linear order in m in the tensors $\hat{\alpha}_m$, $\hat{\alpha}_{nm}$, and $\hat{\alpha}_{mn}$ and terms up to quadratic order in m in $\hat{\alpha}_n$.

Mixing tensors $\hat{\alpha}_{mn}$ and $\hat{\alpha}_{nm}$ must be odd in m , which implies, for our precision, a linear in m approximation. As a result, the sublattice symmetry (the symmetry with respect to renaming A and B) prescribes that the mixing tensors must also be linear in n . In the absence of spin-orbit coupling we are also restricted by spin-rotation invariance that (together with the sublattice and

time-reversion symmetries) dictates the following form of the Gilbert damping contributions to the non-equilibrium spin densities

$$\delta s^+ = \alpha_m \dot{\mathbf{m}} + \alpha'_m \mathbf{n} \times (\mathbf{n} \times \dot{\mathbf{m}}) + \alpha_{mn} \mathbf{m} \times (\mathbf{n} \times \dot{\mathbf{n}}), \quad (3.7a)$$

$$\delta s^- = \alpha_n \dot{\mathbf{n}} + \alpha'_n \mathbf{m} \times (\mathbf{m} \times \dot{\mathbf{n}}) + \alpha_{nm} \mathbf{n} \times (\mathbf{m} \times \dot{\mathbf{m}}), \quad (3.7b)$$

where all coefficients are assumed to be constants.

It is easy to see that the vector forms $\mathbf{n} \times (\mathbf{m} \times \dot{\mathbf{n}})$ and $\mathbf{m} \times (\mathbf{n} \times \dot{\mathbf{m}})$, which could have respectively entered the spin densities δs^+ and δs^- , do not contribute to Eqs. (3.5) in the precision explained above. Substitution of Eqs. (3.7) into Eqs. (3.5) gives

$$\dot{\mathbf{n}} = -\Omega \mathbf{n} \times \mathbf{m} + \mathbf{H} \times \mathbf{n} + \bar{\alpha}_m \mathbf{n} \times \dot{\mathbf{m}} + \alpha_n \mathbf{m} \times \dot{\mathbf{n}}, \quad (3.8a)$$

$$\begin{aligned} \dot{\mathbf{m}} = & \mathbf{H} \times \mathbf{m} + \alpha_n \mathbf{n} \times \dot{\mathbf{n}} \\ & + \bar{\alpha}_m \mathbf{m} \times \dot{\mathbf{m}} + \gamma (\mathbf{n} \times \mathbf{m})(\mathbf{n} \cdot \dot{\mathbf{m}}) - \alpha'_n m^2 \mathbf{n} \times \dot{\mathbf{n}}, \end{aligned} \quad (3.8b)$$

where $\bar{\alpha}_m = \alpha_m - \alpha'_m$ and $\gamma = \alpha_{mn} + \alpha_{nm} + \alpha'_m - \alpha'_n$. Discarding the three last terms in Eq. (3.8b), which are all of the second order in \mathbf{m} , we indeed arrive at a set of Gilbert damping terms that is widely used in the AFM literature [Kamra2018, PhysRevMaterials.1.061401, Yuan_2019].

The symmetry consideration behind Eqs. (3.8) has essentially relied upon the spin-rotation invariance. This also implies $\alpha_n = 0$ as has been pointed out in the introductory section. The coefficient α_m can, in turn, be finite and large, even in the absence of spin-orbit interaction. As we will show below, the presence of spin-orbit interaction does not only provide us with a finite α_n but also drastically change the symmetry structure of Eqs. (3.8). We will demonstrate that the onset of spin-orbit interaction strongly affects the coupling of the localized spin subsystem to the electron bath (described by the tight-binding model) resulting in a strong reduction in the ability of conduction electrons to flip spins in certain directions and, therefore, to impose a friction on magnetization dynamics.

In the following, we turn to the microscopic analysis of the conductivity (Sec. 3.4), spin-orbit torques (Sec. 3.5) and Gilbert dampings (Sec. 3.6) in a particular model of Rashba honeycomb AFM that has been put forward recently by some of the authors [Sumit2019]. Rashba spin-orbit interaction breaks spin-rotational invariance of the model by singling out the direction $\hat{\mathbf{z}}$ perpendicular to the 2D plane. We, therefore, investigate how such spin-rotation breaking manifests itself in the anisotropy of the abovementioned quantities.

3.3 MICROSCOPIC MODEL

For the sake of a microscopic analysis we adopt a sublattice symmetric s-d-like model of a 2D honeycomb antiferromagnet with Rashba spin-orbit coupling,

that was introduced in Ref. Sumit2019. The energy dispersion of this model is illustrated schematically in Fig. 3.2. The low energy model for conduction electrons responsible for the dispersion in Fig. 3.2, is described by an effective Hamiltonian (see Appendix 3.9) that in a valley-symmetric representation reads

$$H^{\text{eff}} = v \mathbf{p} \cdot \boldsymbol{\Sigma} + \frac{1}{2} \lambda [\boldsymbol{\sigma} \times \boldsymbol{\Sigma}]_z - \Delta \mathbf{n} \cdot \boldsymbol{\sigma} \Sigma_z \Lambda_z + V(\mathbf{r}). \quad (3.9)$$

Here $\boldsymbol{\Sigma}$, $\boldsymbol{\Lambda}$, and $\boldsymbol{\sigma}$ are the vectors of Pauli matrices in sublattice, valley and spin space, respectively, v is the characteristic Fermi velocity, while λ and $\Delta = JS$ are the energy scales characterizing the strength of Rashba spin-orbit coupling and s-d-like exchange energy, correspondingly.

The term $V(\mathbf{r})$ stands for a scalar Gaussian white-noise disorder potential, which is proportional to the unit matrix in sublattice, valley and spin space. The potential has a zero mean value $\langle V(\mathbf{r}) \rangle = 0$ and is fully characterized by the pair correlator,

$$\langle V(\mathbf{r}) V(\mathbf{r}') \rangle = 2\pi(\hbar v)^2 \alpha_d \delta(\mathbf{r} - \mathbf{r}'), \quad (3.10)$$

where the angular brackets denote the averaging over disorder realizations. The dimensionless parameter $\alpha_d \ll 1$ quantifies the disorder strength.

The disorder potential is responsible for a momentum relaxation of conduction electrons. Exchange interaction and spin-orbit scattering (or the scattering on a non-collinear configurations with $\mathbf{m} \neq 0$) enable coupling between localized angular momenta and kinetic momenta of electrons. Together these mechanisms form a channel to dissipate angular momentum of localized spins into the lattice. Thus, our model provides us with a microscopic framework to study dissipative quantities such as Gilbert dampings, anti-damping spin-orbit torques and conductivity that we compute below. We also note that the computation of spin-relaxation time can be directly related to our analysis of Gilbert damping [Hankiewicz2007, Manchon2017].

The spectrum of the model (3.9) with $V(\mathbf{r}) = 0$ consists of two electron and two hole branches for each of the valleys as illustrated in Fig. 3.2,

$$\epsilon_{\pm, \sigma}^e(\mathbf{p}) = \sqrt{v^2 \mathbf{p}^2 + \Delta^2 \pm \sigma \lambda \Delta n_z + \lambda^2/4} \mp \lambda/2, \quad (3.11a)$$

$$\epsilon_{\pm, \sigma}^h(\mathbf{p}) = -\sqrt{v^2 \mathbf{p}^2 + \Delta^2 \mp \sigma \lambda \Delta n_z + \lambda^2/4} \pm \lambda/2, \quad (3.11b)$$

where $\sigma = \pm$ is the valley index. All spectral branches are manifestly isotropic with respect to the direction of the electron momentum \mathbf{p} irrespective of the Néel vector orientation (as far as $\mathbf{m} = 0$).

In order to limit the complexity of our microscopic analysis we restrict ourselves to the metallic regime that corresponds to the Fermi energy $\epsilon_F > \Delta + \lambda$ above the minimum of the top electron branches, $\epsilon_{+, \sigma}^e(\mathbf{p})$, as shown schematically in

Fig. 3.2. Note that the Fermi energy ε_F is counted in the model from the center of the AFM gap. We also focus on the limit of weak disorder $\varepsilon_F\tau/\hbar \gg 1$ where $\tau = \hbar/(\pi\alpha_d\varepsilon_F)$ stands for the electron scattering time. Also, in order to describe spin-orbit induced anisotropy we find it convenient to decompose the Néel vector (as well as the magnetization vector) to the in-plane and perpendicular-to-the-plane components as $\mathbf{n} = \mathbf{n}_{\parallel} + \mathbf{n}_{\perp}$, where $\mathbf{n}_{\perp} = n_z\hat{z}$.

3.4 CONDUCTIVITY

The electric conductivity in the metallic regime is dominated by electron diffusion. Despite the fact that the Fermi surface (line) is isotropic and does not depend on the direction of \mathbf{n}_{\parallel} , the conductivity appears to be weakly anisotropic with respect to in-plane rotations of the Néel vector due to the onset of spin-orbit interaction. In particular, for $n_z = 0$ we find the diagonal conductivity components

$$\sigma_{xx} = \frac{4e^2}{h} \frac{\varepsilon_F\tau}{\hbar} \frac{\varepsilon_F^2 - \Delta^2}{\varepsilon_F^2 + 3\Delta^2}, \quad (3.12a)$$

$$\sigma_{yy} = \sigma_{xx} + \frac{4e^2}{h} \frac{\varepsilon_F\tau}{\hbar} \frac{\varepsilon_F^2}{\varepsilon_F^2 + \Delta^2} \frac{\lambda^2\Delta^2}{\varepsilon_F^4 + \varepsilon_F^2\Delta^2 + 2\Delta^4}, \quad (3.12b)$$

where the principal axes correspond to choosing \hat{x} direction along \mathbf{n}_{\parallel} (see Fig. 3.1). In the deep metal regime, and for a general direction of \mathbf{n} , this anisotropy is evidently small

$$\frac{\rho_{xx} - \rho_{yy}}{\rho_{xx} + \rho_{yy}} = \frac{\lambda^2\Delta^2}{\varepsilon_F^4} (1 - n_z^2), \quad \varepsilon_F \gg \lambda + \Delta, \quad (3.13)$$

where $\rho_{\alpha\alpha} = 1/\sigma_{\alpha\alpha}$ is the corresponding resistivity tensor component. We note that the anomalous Hall conductivity is identically vanishing in the model of Eq. (3.9).

The results of Eq. (3.12) and all subsequent results of our paper are technically obtained from linear response Kubo formulas evaluated in the diffusive approximation (ladder diagram summation). The details of these calculations can be found in Appendixes 3.10, 3.11, and 3.12.

3.5 SPIN-ORBIT TORQUE

Before proceeding with the microscopic analysis of Gilbert damping we shall discuss the effects of spin-orbit induced anisotropy for spin-orbit torques in the model of Eq. (3.9). Since this anisotropy appears to be weak in the metal regime, we shall touch on it only briefly.

As was already mentioned, the spin-orbit torques originate in the response of nonequilibrium spin polarizations δs^\pm to electric current. Technically, we compute first the response of δs^\pm to electric field and, then, express the electric field in terms of 2D electric current density \mathbf{j} using the conductivity tensor of Eq. (3.12).

A straightforward computation of such a response gives $\delta s^- = 0$ (see Appendixes 3.10 and 3.11 for more detail) and

$$\begin{aligned} \delta s^+ = & a(n_z^2) \hat{\mathbf{z}} \times \mathbf{j} + b(n_z^2) \mathbf{n}_\parallel \times (\mathbf{n}_\parallel \times (\hat{\mathbf{z}} \times \mathbf{j})) \\ & + c(n_z^2) \mathbf{n}_\parallel \times (\mathbf{n}_\perp \times (\hat{\mathbf{z}} \times \mathbf{j})), \end{aligned} \quad (3.14)$$

where the coefficients a , b and c do generally depend on $n_z^2 = 1 - n_x^2 - n_y^2$ and are shown in Fig. 3.3. It is appropriate to recall here that the computation of the responses from the model of Eq. (3.9) refers to the case when $\mathbf{m} = 0$. The symmetry form of Eq. (3.14) in this case has been also established recently from numerical simulations [Sumit2019].

Importantly, the first term in the right-hand side of Eq. (3.14) represents the well-known Rashba-Edelstein effect [Edelstein1990], while the other two terms represent higher harmonics of the same field-like effect that arise due to spin-rotation symmetry breaking. Anti-damping like torques (that are even under time-reversal) are vanishing in the model due to the valley symmetry constraint. This symmetry reads $\Lambda_x H[\mathbf{n}] \Lambda_x = H[-\mathbf{n}]$, from which it follows that the response of δs^+ to charge current must be an even function of \mathbf{n} .

The behavior of the coefficients a , b and c as a function of n_z is illustrated in Fig. 3.3 for two different choices of the Fermi energy. For in-plane Néel vector orientations ($n_z = 0$) we find

$$a = a_0 \frac{1 + 3\delta^2}{1 + 2\bar{\lambda}^2\delta^2 + \delta^4 - 2\delta^6}, \quad (3.15a)$$

$$b = 2a\delta^2 \frac{1 - 2\bar{\lambda}^2 - 4\delta^2 + \delta^4}{1 + 2\delta^2 - 3\delta^4}, \quad (3.15b)$$

$$c = -2a\delta^2 \frac{1 + 2\bar{\lambda}^2\delta^2 - 2\delta^2 - 3\delta^4 - 4\delta^6}{1 + 4\delta^2 + 5\delta^4 + 6\delta^6}, \quad (3.15c)$$

where

$$a_0 = \frac{\mathcal{A}J}{e\hbar v} \frac{\lambda}{\varepsilon_F}, \quad \bar{\lambda} = \frac{\lambda}{\varepsilon_F}, \quad \delta = \frac{\Delta}{\varepsilon_F}. \quad (3.16)$$

In the metal regime, $\varepsilon_F \gg \lambda + \Delta$, the results of Eqs. (3.15) are reduced to

$$a = \frac{\mathcal{A}J}{e\hbar v} \frac{\lambda}{\varepsilon_F}, \quad b = -c = 2 \frac{\mathcal{A}J}{e\hbar v} \frac{\lambda}{\varepsilon_F} \left(\frac{\Delta}{\varepsilon_F} \right)^2. \quad (3.17)$$

Figure 3.3: The coefficients a , b , and c in Eq. (3.14) as a function of the direction of the Néel vector, $n_z = \cos \theta$, for two different Fermi energies: $\varepsilon_F = 4\Delta$ (left panel) and $\varepsilon_F = 16\Delta$ (right panel). We use $\lambda = 1.5\Delta$. For $n_z = 0$ the results correspond to Eqs. (3.15).

One can, therefore, see that the high harmonics terms (proportional to b and c) become irrelevant in the metal regime.

Vanishing response of the staggered polarization, $\delta s^- = 0$, for the model of Eq. (3.9) is a simple consequence of the sublattice symmetry. As shown below the presence of a finite, though small, \mathbf{m} breaks such a symmetry and leads to a finite δs^- . Taking into account a linear in \mathbf{m} term in the Hamiltonian is also necessary to obtain finite mixed Gilbert damping tensors $\hat{\alpha}_{nm}$ and $\hat{\alpha}_{mn}$ in Eq. (3.6).

A low-energy model that takes into account finite magnetization vector reads (see also Appendix 3.12)

$$H = H^{\text{eff}} - \Delta \mathbf{m} \cdot \boldsymbol{\sigma}, \quad (3.18)$$

where H^{eff} is given by Eq. (3.9). The conductivity tensor does not acquire a linear in \mathbf{m} terms in the leading order with respect to the large metal parameter $\varepsilon_F \tau / \hbar$, because the anomalous Hall effect remains subleading with respect to the metal parameter. Similarly, the result of Eq. (3.14) is not affected by the linear in \mathbf{m} corrections.

However, the direct computation of the staggered polarization response (in the linear order with respect to \mathbf{m}) gives rise to a finite result. In the limit of large Fermi energy $\varepsilon_F \gg \lambda + \Delta$, we find

$$\begin{aligned} \delta s^- = \frac{AJ}{e\hbar v} \frac{\lambda}{\varepsilon_F} \left(\frac{\Delta}{\varepsilon_F} \right)^2 & \left[2 \mathbf{n}_\perp \times (\mathbf{m}_\perp \times (\hat{\mathbf{z}} \times \mathbf{j})) \right. \\ & \left. + 2 \mathbf{m}_\parallel \times (\mathbf{n}_\perp \times (\hat{\mathbf{z}} \times \mathbf{j})) - 3 \mathbf{n}_\parallel \times (\mathbf{m}_\perp \times (\hat{\mathbf{z}} \times \mathbf{j})) \right], \end{aligned} \quad (3.19)$$

where the overall strength of the effect is again of the order of the coefficients b and c . This makes the effects of nonequilibrium staggered polarization (including the celebrated Néel spin-orbit torque) irrelevant in the metal regime. Indeed, staggered polarization can hardly be induced by electrons with wavelengths that strongly exceed the distance between A and B sublattices.

The results of Eqs. (3.14), (3.15) clearly suggest that the only torques surviving in the large energy limit are those related to non-equilibrium polarization $\delta \mathbf{s}_+ = a_0 \hat{\mathbf{z}} \times \mathbf{j}$, which is nothing but the standard Rashba-Edelstein effect [Edelstein1990]. These torques have a form $\mathbf{T}_n = a_0 \mathbf{n} \times (\hat{\mathbf{z}} \times \mathbf{j})$ in the right-hand side of Eq. (3.5a) and $\mathbf{T}_m = a_0 \mathbf{m} \times (\hat{\mathbf{z}} \times \mathbf{j})$ in the right-hand side of Eq. (3.5b). The anisotropy of torques is, however, irrelevant in this limit.

3.6 GILBERT DAMPING

Surprisingly, the situation is different when we consider Gilbert damping terms. In this case we find that the giant anisotropy of Gilbert damping persists to arbitrarily large Fermi energy as soon as spin orbit energy λ exceeds \hbar/τ . The latter condition ensures that the scattering between spin-split subbands is suppressed.

The direct computation of the Gilbert damping tensors for $\lambda \gg \hbar/\tau$ gives

$$\delta s^+ = \alpha_m^\parallel \dot{\mathbf{m}}_\parallel + \gamma \mathbf{\Gamma}_{mm} + \gamma \mathbf{\Gamma}_{mn}, \quad (3.20a)$$

$$\delta s^- = \alpha_n^\perp \dot{\mathbf{n}}_\perp + \gamma \mathbf{\Gamma}_{nm} + \gamma \mathbf{\Gamma}_{nn}, \quad (3.20b)$$

where the terms $\mathbf{\Gamma}_{ab}$ contain various vector forms.

Far in the metal regime, $\varepsilon_F \gg \lambda + \Delta$, we find

$$\alpha_m^\parallel = 2 \frac{\varepsilon_F \tau}{\hbar} \frac{AJ^2 S}{\pi \hbar^2 v^2} \left[1 - \frac{\Delta^2}{\varepsilon_F^2} (2 + n_z^2) + \dots \right], \quad (3.21a)$$

$$\alpha_n^\perp = \frac{\varepsilon_F \tau}{\hbar} \frac{AJ^2 S}{\pi \hbar^2 v^2} \left[\left(\frac{\lambda}{\varepsilon_F} \right)^2 + \dots \right], \quad (3.21b)$$

$$\gamma = 2 \frac{\varepsilon_F \tau}{\hbar} \frac{AJ^2 S}{\pi \hbar^2 v^2} \left[\left(\frac{\Delta}{\varepsilon_F} \right)^2 + \dots \right], \quad (3.21c)$$

while the vectors forms $\mathbf{\Gamma}_{ab}$ can be written as

$$\begin{aligned} \mathbf{\Gamma}_{mm} = & \mathbf{n} \times (\mathbf{n} \times \dot{\mathbf{m}}) + \mathbf{n}_\parallel \times (\mathbf{n}_\parallel \times \dot{\mathbf{m}}_\parallel) \\ & - 2\mathbf{n}_\parallel \times (\mathbf{n}_\parallel \times \dot{\mathbf{m}}_\perp), \end{aligned} \quad (3.22a)$$

$$\begin{aligned} \mathbf{\Gamma}_{mn} = & \mathbf{n} \times (\mathbf{m}_\parallel \times \dot{\mathbf{n}}_\perp) - \mathbf{m}_\perp \times (\mathbf{n}_\parallel \times \dot{\mathbf{n}}_\perp) \\ & + \mathbf{n}_\perp \times (\mathbf{m}_\perp \times \dot{\mathbf{n}}_\parallel) - \mathbf{n}_\parallel \times (\mathbf{m}_\parallel \times \dot{\mathbf{n}}_\parallel) \\ & - 3\mathbf{m}_\perp \times (\mathbf{n}_\perp \times \dot{\mathbf{n}}_\parallel), \end{aligned} \quad (3.22b)$$

$$\begin{aligned} \mathbf{\Gamma}_{nm} = & 2\mathbf{n}_\parallel \times (\mathbf{m}_\parallel \times \dot{\mathbf{n}}_\perp) + 2\mathbf{m}_\parallel \times (\mathbf{n}_\perp \times \dot{\mathbf{m}}_\parallel) \\ & - \mathbf{n}_\perp \times (\mathbf{m}_\perp \times \dot{\mathbf{m}}) + 2\mathbf{m}_\perp \times (\mathbf{n} \times \dot{\mathbf{m}}) \\ & + \mathbf{m}_\parallel \times (\mathbf{n} \times \dot{\mathbf{m}}_\perp) - \mathbf{m}_\perp \times (\mathbf{n}_\perp \times \dot{\mathbf{m}}_\parallel), \end{aligned} \quad (3.22c)$$

$$\mathbf{\Gamma}_{nn} = -\mathbf{m} \times (\mathbf{n} \times \dot{\mathbf{n}}_\parallel). \quad (3.22d)$$

Thus, we see from Eqs. (3.21) that the coefficients α_n^\perp and γ are vanishingly small in the metal regime. Moreover, in the limit $\varepsilon_F \gg \Delta$ the only non-vanishing contributions to Gilbert dampings are given by the first terms on the right-hand sides of Eqs. (3.20) that are manifestly anisotropic.

The onset of spin-orbit interactions therefore makes Gilbert dampings ultimately anisotropic, also in the deep metal regime. This is in contrast to conductivity and spin-orbit torques that are quickly becoming isotropic in the metal limit. For $\varepsilon_F \gg \lambda + \Delta$, we find the well known Landau-Lifshitz-Gilbert equations

$$\begin{aligned}\dot{\mathbf{n}} &= -\Omega \mathbf{n} \times \mathbf{m} + \mathbf{H} \times \mathbf{n} + \bar{\alpha}_m^{\parallel} \mathbf{n} \times \dot{\mathbf{m}}_{\parallel} + \alpha_n^{\perp} \mathbf{m} \times \dot{\mathbf{n}}_{\perp}, \\ \dot{\mathbf{m}} &= \mathbf{H} \times \mathbf{m} + \alpha_n^{\perp} \mathbf{n} \times \dot{\mathbf{n}}_{\perp} + \bar{\alpha}_m^{\parallel} \mathbf{m} \times \dot{\mathbf{m}}_{\parallel},\end{aligned}\quad (3.23)$$

where we again omit terms that originate e. g. from magnetic anisotropy of the AFM. Eqs. (3.23) are clearly different from Eqs. (3.8) derived on the basis of symmetry analysis in the absence of spin-orbit interaction.

The very pronounced, highly anisotropic Gilbert damping terms in the Landau-Lifshitz-Gilbert equations of Eqs. (3.23) represent the main result of our paper. The phenomenon of the giant Gilbert damping anisotropy in the 2D AFM clearly calls for a qualitative understanding that we provide in Sec. 3.7.

3.7 QUALITATIVE CONSIDERATION

The results of Eqs. (3.20), (3.21) suggest that the anisotropy of Gilbert damping is most pronounced in the metal limit, $\varepsilon_F \gg \Delta + \lambda$ as far as $\lambda\tau/\hbar \gg 1$. In particular, certain spin density responses are vanishing in this limit. One of them is the response of the average spin density δs_z^+ to \dot{m}_z that is defined by the tensor component α_m^{zz} in Eq. (3.6). The other four vanishing tensor components α_n^{xx} , α_n^{xy} , α_n^{yx} and α_n^{yy} correspond to the responses of the in-plane staggered spin densities δs_x^- and δs_y^- to \dot{n}_x and \dot{n}_y .

It is important to stress that the component α_m^{zz} is not only finite but also quite large in the absence of spin-orbit interaction, i. e. for $\lambda = 0$. It is, therefore, instructive to understand how the onset of spin-orbit interaction may cancel α_m^{zz} response and lead to the conservation of z projection of magnetization vector.

Such a qualitative understanding can be achieved by considering the Kubo-Greenwood formula for α_m^{zz} for the model of Eq. (3.18) in the limit $\Delta \rightarrow 0$ and $\tau \rightarrow \infty$,

$$\alpha_m^{zz} \propto \sum_{\mathbf{p}} \sum_{s,s'=\pm} |\langle \Psi_{\mathbf{p},s} | \sigma_z | \Psi_{\mathbf{p},s'} \rangle|^2 \delta(\varepsilon_F - \epsilon_{\mathbf{p},s}^e) \delta(\varepsilon_F - \epsilon_{\mathbf{p},s'}^e), \quad (3.24)$$

where $\epsilon_{\mathbf{p},\pm}^e = \sqrt{v^2 p^2 + \lambda^2/4} \mp \lambda/2$ correspond to the two electronic branches of Eq. (3.11a) that are evidently valley degenerate in the limit $\Delta \rightarrow 0$.

The states $\Psi_{\mathbf{p},s}$ are simply the eigenstates of the Hamiltonian $H_0 = v\mathbf{p} \cdot \boldsymbol{\Sigma} + (\lambda/2) [\boldsymbol{\sigma} \times \boldsymbol{\Sigma}]_z$,

$$H_0 = \begin{pmatrix} 0 & 0 & v(p_x - ip_y) & 0 \\ 0 & 0 & -i\lambda & v(p_x - ip_y) \\ v(p_x + ip_y) & i\lambda & 0 & 0 \\ 0 & v(p_x + ip_y) & 0 & 0 \end{pmatrix}, \quad (3.25)$$

that can be explicitly written as

$$\Psi_{\mathbf{p},\pm} = \frac{1}{2\sqrt{v^2 p^2 \mp \lambda \epsilon_{\pm}^e}/2} \begin{pmatrix} vp e^{-i\phi} \\ \pm i \epsilon_{\pm}^e \\ \epsilon_{\pm}^e \\ \pm ivp e^{i\phi} \end{pmatrix}, \quad (3.26)$$

where we have used $p_x = p \cos \phi$, $p_y = p \sin \phi$.

One may notice that $\langle \Psi_{\mathbf{p},s} | \sigma_z | \Psi_{\mathbf{p},s} \rangle = 0$ for any value of λ suggesting that the response function α_m^{zz} in Eq. (3.24) is vanishing. This is, however, not the case for $\lambda = 0$. Indeed, in the absence of spin-orbit interaction the electron branches become degenerate $\epsilon_{\mathbf{p},\pm}^e = vp$ such that the in-plane spin-flip processes contribute to the Kubo formula,

$$\langle \Psi_{\mathbf{p},+} | \sigma_z | \Psi_{\mathbf{p},-} \rangle \big|_{\lambda=0} = \langle \Psi_{\mathbf{p},-} | \sigma_z | \Psi_{\mathbf{p},+} \rangle \big|_{\lambda=0} = 1. \quad (3.27)$$

These processes are exactly the ones responsible for a finite Gilbert damping component α_m^{zz} in the absence of spin-orbit interaction. The spin-orbit induced splitting of the subbands forbids these spin-flip processes as soon as $\lambda\tau/\hbar \gg 1$ and leads to a giant anisotropy of Gilbert damping in the metal limit. Indeed, the other elements of the Gilbert damping tensor α_m^{xx} and α_m^{yy} remain finite irrespective of the subband splitting,

$$\langle \Psi_{\mathbf{p},\pm} | (\sigma_x + i\sigma_y) | \Psi_{\mathbf{p},\pm} \rangle = \frac{\pm ivp e^{i\phi}}{\sqrt{v^2 p^2 + \lambda^2/4}}. \quad (3.28)$$

One can further show that for $\lambda = 0$ the entire Gilbert damping tensor $\hat{\alpha}_m$ becomes isotropic $\hat{\alpha}_m^{xx} = \hat{\alpha}_m^{yy} = \hat{\alpha}_m^{zz}$ as it have been expected on the basis of the symmetry analysis.

Very similar physics is also responsible for the anisotropy of the tensor $\hat{\alpha}_n$. It is worth noting that the same type of anisotropy is known to take place in the limit of large spin-orbit interaction in 2D Rashba ferromagnets [AdoSTTGD2019]. Spin-orbit induced anisotropy of Gilbert damping plays, however, a lesser role in 2D ferromagnets due to the much stricter constraint on the single magnetization

vector. A less restricted dynamics of \mathbf{m} and \mathbf{n} vectors make the Gilbert damping anisotropy play a bigger role in 2D AFMs.

Indeed, it can be directly seen from Eqs. (3.23) that a nonequilibrium state with $\mathbf{m} = m\hat{z}$ and $\mathbf{n} = \mathbf{n}_{\parallel}$ becomes undamped in the absence of external field $\mathbf{H} = 0$. Such a state corresponds to the undamped Néel vector precession around \hat{z} axis with a frequency given by $J_{\text{ex}}m$. The state clearly survives in the presence of easy plane magnetic anisotropy in the AFM. We believe that such a phenomenon remains to be rather generic for a variety of 2D or layered AFM systems with strong spin-orbit coupling of Rashba type.

3.8 CONCLUSIONS

In this paper, we demonstrate that the presence of sufficiently strong spin-orbit coupling $\lambda\tau/\hbar \gg 1$ results in the ultimate anisotropy of the Gilbert damping tensor in the metal regime, $\varepsilon_F \gg \Delta + \lambda$. One can trace the phenomenon to the spin-orbit induced splitting of Fermi surfaces that forbids scattering processes that are responsible for the relaxation of certain magnetization and Néel vector components.

We also demonstrate that a finite in-plane projection \mathbf{n}_{\parallel} of the Néel vector is responsible for a weak anisotropy of conductivity and spin-orbit torques for Fermi energies approaching the band edge, $\varepsilon_F \sim \Delta + \lambda$. This anisotropy is, however, absent in the metallic regime.

Gilbert damping is, however, in the absence of spin-orbit interaction as it is required by symmetry considerations. Thus, we demonstrate that the onset of Rashba spin-orbit interaction in 2D or layered AFM systems leads to a giant anisotropy of Gilbert damping in the metallic regime. The physics of this phenomenon originates in spin-orbit induced splitting of the electron subbands that destroys a particular decay channel for magnetization and leads to undamped precession of the Néel vector. The phenomenon is based on the assumption that other Gilbert damping channels (e. g. due to phonons) remain suppressed in the long magnon wavelength limit that we consider. The predicted giant Gilbert damping anisotropy may have a profound impact on the Néel vector dynamics in a variety of 2D and layered AFM materials.

3.9 MODEL SYSTEM

In this Appendix, we shall briefly justify Eqs. (3.9) and (3.18) of the main text. We start from an s-d-like model for two-dimensional antiferromagnet on a honeycomb lattice [Sumit2019]. The model includes a local exchange interaction between localized magnetic moments and conduction electron spins as given

by Eq. (3.1). Itinerant electrons in the model are, therefore, governed by the tight-binding Hamiltonian

$$H_0 = -t \sum_i \sum_{\sigma\sigma'} c_{i\sigma}^\dagger c_{i\sigma'} - J \sum_i \sum_{\sigma\sigma'} \mathbf{S}_i \cdot \boldsymbol{\sigma}_{\sigma\sigma'} c_{i\sigma}^\dagger c_{i\sigma'} + \frac{i\lambda}{3a} \sum_{\langle i,j \rangle} \sum_{\sigma\sigma'} \hat{\mathbf{z}} \cdot (\boldsymbol{\sigma} \times \mathbf{d}_{ij})_{\sigma\sigma'} c_{i\sigma}^\dagger c_{j\sigma'}, \quad (3.29)$$

where we do ignore disorder for a moment. The model is characterized by the nearest neighbor hopping energy t and the Rashba spin-orbit coupling energy λ , z -axis is aligned perpendicular to the two-dimensional plane, the in-plane vectors \mathbf{d}_{ij} connect the neighboring sites i and j on a honeycomb lattice. For any site i on the sublattice A we choose

$$\mathbf{d}_1 = a \begin{pmatrix} 0 \\ 1 \end{pmatrix}, \quad \mathbf{d}_2 = \frac{a}{2} \begin{pmatrix} \sqrt{3} \\ -1 \end{pmatrix}, \quad \mathbf{d}_3 = -\frac{a}{2} \begin{pmatrix} \sqrt{3} \\ 1 \end{pmatrix}, \quad (3.30)$$

where a is the length of the bond between A and B .

By projecting the tight-binding model of Eq. (3.29) on states in a vicinity of the valley wave-vectors,

$$\mathbf{K} = \frac{4\pi}{3\sqrt{3}a} \begin{pmatrix} 1 \\ 0 \end{pmatrix}, \quad \text{and} \quad \mathbf{K}' = -\mathbf{K}, \quad (3.31)$$

we find, in the valley symmetric approximation, the effective Hamiltonian of Eq. (3.9) with the assumption that $\mathbf{S}^A = -\mathbf{S}^B$, where $v = 3ta/2\hbar$. By relaxing the assumption we obtain the model of Eq. (3.18).

3.10 LINEAR RESPONSE TENSORS

In order to keep technical expressions compact we let $\hbar = 1$ and $\varepsilon_F = \varepsilon$ below. Our technical analysis is based on linear response of electron spin density to various perturbations at zero frequency (dc) limit. In particular, we consider three types of responses: the one with respect to electric current (via electric field and inverse conductivity tensor), the one with respect to the time derivative of the Néel vector and the other one with respect to the time derivative of magnetization vector. These responses are summed up as

$$\delta \mathbf{s}^+ = \hat{\mathbf{S}}_+^{\text{SOT}} \mathbf{j} + \hat{\mathbf{S}}_{mn}^{\text{GD}} \dot{\mathbf{n}} + \hat{\mathbf{S}}_m^{\text{GD}} \dot{\mathbf{m}}, \quad (3.32a)$$

$$\delta \mathbf{s}^- = \hat{\mathbf{S}}_-^{\text{SOT}} \mathbf{j} + \hat{\mathbf{S}}_{nm}^{\text{GD}} \dot{\mathbf{m}} + \hat{\mathbf{S}}_n^{\text{GD}} \dot{\mathbf{n}}, \quad (3.32b)$$

where we define the response tensors $\hat{\mathbf{S}}_\pm^{\text{SOT}}$ that are describing spin-orbit torques (both field-like and anti-damping) and various $\hat{\mathbf{S}}^{\text{GD}}$ tensors that are describing

various contributions to Gilbert dampings (and to effective spin renormalizations) [AdoSTTGD2019].

In order to compute the linear response tensors in Eqs. (3.32) we apply the standard Kubo formula

$$\delta s_{\alpha}^{\pm} = \frac{J^2 S v^2 \mathcal{A}}{2V} \sum_{\beta} \widehat{\text{Tr}} \left\langle \hat{G}_{\alpha}^{\text{R} \pm} \hat{G}_{\beta}^{\text{A}} \hat{\mathbf{F}}_{\beta} \right\rangle \frac{\partial X_{\beta}}{\partial t}, \quad (3.33)$$

where V is the system area, $\widehat{\text{Tr}}$ is an operator trace, $\hat{G}^{\text{R(A)}} = (\varepsilon - H \pm i0)$ are retarded (advanced) Green function operators, $\hat{s}_{\alpha}^{+} = \sigma_{\alpha}$, $\hat{s}_{\alpha}^{-} = \Lambda_z \Sigma_z \sigma_{\alpha}$ are the operators corresponding to the average spin-polarization s^{+} and staggered spin-polarization s^{-} , the product $\hat{\mathbf{F}} \cdot \mathbf{X}(t)$ represents the time-dependent perturbation in the Hamiltonian, while the angular brackets denote the disorder averaging that we consider in diffusive (ladder) approximation.

The linear-response formula Eq. (3.33) assumes zero temperature and zero frequency limit that corresponds to taking both Green's functions at the same energy $\varepsilon = \varepsilon_{\text{F}}$. We also neglect the Fermi-sea contribution (also known as Středa contribution) since such a contribution appears to be either zero or subleading in the metal parameter $\varepsilon\tau \gg 1$ with respect to our results.

Thus, in order to compute Gilbert dampings and spin-orbit torque tensors we consider linear response of δs^{\pm} to the three perturbations mentioned above. Each perturbation is parameterized by the term $\delta H = \hat{\mathbf{F}} \cdot \mathbf{X}(t)$ with

$$\dot{\mathbf{X}} = \dot{\mathbf{n}}, \quad \hat{\mathbf{F}} = -\Delta \Lambda_z \Sigma_z \sigma, \quad (3.34a)$$

$$\dot{\mathbf{X}} = \dot{\mathbf{m}}, \quad \hat{\mathbf{F}} = -\Delta \sigma, \quad (3.34b)$$

$$\dot{\mathbf{X}} = (\pi v/e) \hat{\sigma}^{-1} \mathbf{j}, \quad \hat{\mathbf{F}} = \Sigma, \quad (3.34c)$$

where $\hat{\sigma}$ is the conductivity tensor (this is computed from the standard Kubo formula which is analogous to the one in Eq. (3.33) but for the response of current density to electric field). The disorder averaging amounts to replacing Green's functions in Eq. (3.33) with the corresponding disorder-averaged Green's functions and to replacing one of the operators, \hat{s}_{α} or $\hat{\mathbf{F}}$, with the corresponding vertex-corrected operator.

Disorder-averaged Green's functions become diagonal in the momentum space due to restored translational invariance and take the form $G_p^{\text{R(A)}} = [\varepsilon - H - \Sigma^{\text{R(A)}}]^{-1}$, where the Hamiltonian H is defined in Eq. (3.9) of the main text, while the self-energy $\Sigma^{\text{R(A)}}$ is evaluated in the Born-approximation depicted schematically in Fig. 3.4a.

We find that the real part of the self-energy does renormalize the Fermi energy ε and the s-d exchange coupling strength Δ , while the imaginary part reads

$$\text{Im } \Sigma^{\text{R(A)}} = \mp \frac{\pi \alpha_{\text{d}}}{2} (\varepsilon - \Delta \Lambda_z \Sigma_z \mathbf{n} \cdot \boldsymbol{\sigma}). \quad (3.35)$$

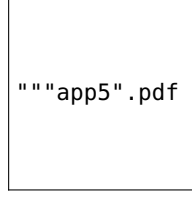


Figure 3.4: Diagrammatic illustration. a) Born-approximation. b) Ladder-approximation. c) Disorder-averaged polarization bubble. d) Perturbative expansion of the disorder-averaged polarization bubble.

In order to evaluate linear response tensors in the leading order with respect to the metal parameter $\varepsilon\tau \gg 1$ one also needs to sum up the ladder diagrams as shown in Fig. 3.4b-c.

To do that one defines the vertex corrected operator

$$\hat{F}^{vc} = \hat{F} + \hat{F}^{(1)} + \hat{F}^{(2)} + \hat{F}^{(3)} + \dots, \quad (3.36)$$

where we denote by $\hat{F}^{(i)}$ the operator \hat{F} that is dressed by the number of i disorder lines,

$$\hat{F}^{(i)} = 2\pi\alpha_d \int \frac{d^2\mathbf{p}}{(2\pi)^2} G_{\mathbf{p}}^R \hat{F}^{(i-1)} G_{\mathbf{p}}^A. \quad (3.37)$$

It appears that the summation in Eq. (3.36) can be reduced to geometric series in a finite operator space. Indeed, let us define the operator space that is spanned by 16 operators in each of the valleys

$$B_i = \frac{1}{2} \Lambda_{\zeta} \Sigma_{\alpha} \sigma_{\beta}, \quad i = \{\zeta, \alpha, \beta\}, \quad (3.38)$$

where i is a cumulative index with $\zeta = 0, z$ a valley parity index and α, β taking on the four values $\{0, x, y, z\}$ each.

For $\mathbf{B} = (B_1, B_2, \dots, B_{32})$ we define the vertex corrected operator vector as

$$\mathbf{B}^{vc} = \mathbf{B} + \mathcal{F}\mathbf{B} + \mathcal{F}^2\mathbf{B} + \mathcal{F}^3\mathbf{B} + \dots = \frac{1}{1 - \mathcal{F}}\mathbf{B}, \quad (3.39)$$

where \mathcal{F} stands for a matrix of vertex corrections. Using the normalization condition $\text{Tr } B_i B_j = 2\delta_{ij}$ we find

$$\mathcal{F}_{ij} = \pi\alpha_d \int \frac{d^2\mathbf{p}}{(2\pi)^2} \text{Tr} \left[G_{\mathbf{p}}^A B_i G_{\mathbf{p}}^R B_j \right], \quad (3.40)$$

where Tr stands for the usual matrix trace in the valley, spin and sublattice spaces.

It is easy to imagine that the matrix inversion in Eq. (3.39) might be a daunting analytical task. We note, however, that the matrix \mathcal{F} is evidently diagonal in the valley space, and it can also become block-diagonal in sublattice and spin spaces by choosing a more convenient basis.

A particularly useful choice of basis corresponds to in-plane rotation of both spin and sublattice Pauli matrices to the frame associated with the in-plane projection \mathbf{n}_{\parallel} of the Néel vector. For spin Pauli matrices this transformation is given by

$$\sigma_x \rightarrow \Lambda_z \frac{n_x \sigma_x + n_y \sigma_y}{\sqrt{n_x^2 + n_y^2}}, \quad \sigma_y \rightarrow \Lambda_z \frac{n_y \sigma_x - n_x \sigma_y}{\sqrt{n_x^2 + n_y^2}}, \quad (3.41)$$

where we took advantage of the fact that the direction of \mathbf{n} is opposite in the two valleys. The same transformation (3.41) has to be applied to Σ_x and Σ_y .

The matrix \mathcal{F} is instrumental for the analysis of all linear response tensors in Eq. (3.32). Indeed, using the definition of Eq. (3.40) in Eq. (3.33) and summing up the diffusion ladders we find

$$\delta s_{\alpha}^{\pm} = \frac{J^2 S v^2 \mathcal{A}}{2\pi\alpha_d} \sum_{\beta} \sum_{ij} \text{Tr}[\hat{s}_{\alpha}^{\pm} B_i] \mathcal{R}_{ij} \text{Tr}[\hat{f}_{\beta} B_j] \frac{\partial X_{\beta}}{\partial t}, \quad (3.42)$$

where $\mathcal{R} = \mathcal{F}(1 - \mathcal{F})^{-1}$. Thus, the computation of all response tensors is reduced in the diffusive approximation to the computation of the vertex correction matrix \mathcal{F} and subsequent matrix inversion.

3.11 VERTEX CORRECTION

Still, finding an inverse matrix $(1 - \mathcal{F})^{-1}$ is not that straightforward due to a pair of eigenvalues (one per valley) that equal exactly 1. The presence of such eigenvalues roots in the particle conservation and is, therefore, not an artificial problem. The unit eigenvalues do evidently prevent the matrix inversion in Eq. (3.39). Nevertheless, it can be shown that the corresponding eigenvectors do not enter the final equations of motion for localized spins. In the next section, we briefly illustrate how one can formally avoid the particle conservation divergence in the computation of vertex corrections.

Let us define by \mathbf{a}_{ζ} the eigenvectors of \mathcal{F} that correspond to two unit eigenvalues, $\mathcal{F}\mathbf{a}_{\zeta} = \mathbf{a}_{\zeta}$, with $\zeta = 0, z$. For the normalized vector \mathbf{a}_{ζ} we define special operators

$$\bar{B}_{\zeta} = \mathbf{a}_{\zeta} \cdot \mathbf{B} = \frac{\varepsilon - \Delta \Lambda_{\zeta} \Sigma_z \mathbf{n} \cdot \boldsymbol{\sigma}}{2\sqrt{\varepsilon^2 + \Delta^2}}, \quad (3.43)$$

which are conserved with respect to impurity dressing $\bar{B}_\zeta = \bar{B}_\zeta^{(i)}$ for any order i . This means that the vertex corrected operator $\bar{B}_\zeta^{\text{vc}}$ is formally diverging in the dc limit. In what follows, we formally write $\bar{B}_\zeta^{\text{vc}} = R_\infty \bar{B}_\zeta$, where the limit $R_\infty \rightarrow \infty$ is taken at the end of the calculation.

The response tensors defined by Eqs. (3.6) consist of different correlators of the operators Σ_α , $s_\alpha^+ = \sigma_a$, and $s_\alpha^- = \Lambda_z \Sigma_z \sigma_\alpha$. It is evident that most of these operators are already orthogonal to \bar{B}_ζ ,

$$\text{Tr} [\Sigma_\alpha \bar{B}_\zeta] = \text{Tr} [s_\alpha^+ \bar{B}_\zeta] = \text{Tr} [s_\alpha^- \bar{B}_0] = 0, \quad (3.44)$$

while the only dangerous sector is related to the projection

$$\text{Tr} [s_\alpha^- \bar{B}_z] = -\frac{4\Delta n_\alpha}{\sqrt{\epsilon^2 + \Delta^2}}, \quad (3.45)$$

which is evidently finite. The result of Eq. (3.45) leads to formally diverging contribution δs_{div}^- that is generally present in all components of δs^- ,

$$\delta s_{\text{div},\alpha}^- \propto R_\infty \sum_\beta \text{Tr} [\hat{s}_\alpha^- \bar{B}_z] \text{Tr} [\hat{F}_\beta \bar{B}_z] \frac{\partial n_\beta}{\partial t}. \quad (3.46)$$

One can immediately see, however, that such a diverging contribution corresponds to a particular vector form,

$$\delta s_{\text{div},\alpha}^- \propto R_\infty n_\alpha \mathbf{n} \cdot \frac{\partial \mathbf{n}}{\partial t} = 0, \quad (3.47)$$

that manifestly vanishes due to the constraint $|\mathbf{n}| = 1$ which is exact in the limit $m = 0$. Thus, the divergency in $B_{\text{div}}^{\text{vc}}$ (which originates in the diffusion pole of the density-density response) is, in fact, harmless for the response tensors we are discussing.

It is interesting to note that the irrelevance of the divergency in $B_{\text{div}}^{\text{vc}}$ operator extends to higher orders in m , even though it becomes much harder to see. We touch on this problem in Appendix 3.12.

3.12 FINITE MAGNETIZATION

The deviation from a collinear antiferromagnetic order can be accounted by considering a finite net magnetization term in the Hamiltonian perturbatively,

$$H = H^{\text{eff}} + U, \quad U = -\Delta \mathbf{m} \cdot \boldsymbol{\sigma}. \quad (3.48)$$

In the paper, we build the first order perturbation theory with respect to U .

First of all, it can be shown that the self-energy acquires the linear in \mathbf{m} contribution as

$$\text{Im } \Sigma^{R(A)} = \mp \frac{\pi\alpha_d}{2} (\varepsilon - \Delta \wedge_z \Sigma_z \mathbf{n} \cdot \boldsymbol{\sigma} + \Delta \mathbf{m} \cdot \boldsymbol{\sigma}). \quad (3.49)$$

Second, the Dyson expansion of the disorder-averaged Green's functions $G^{R(A)}$ with respect to \mathbf{m} reads

$$G^{R(A)} \rightarrow G^{R(A)} + G^{R(A)} U^{R(A)} G^{R(A)}, \quad (3.50)$$

where $U^{R(A)} = U(1 \pm i\pi\alpha_d/2)$ and we disregarded terms starting from quadratic order in \mathbf{m} . Note, that we have kept the notations $G^{R(A)}$ for the disorder averaged Green's functions of the unperturbed system.

The computation of linear response tensors amounts to considering an additional contribution to the response tensor represented by a complex class of diagrams depicted schematically in Fig. 3.4d. Before ladder summation is applied the diagrams of Fig. 3.4d correspond to a contribution to the correlator of two operators B_i and B_j of the type

$$\begin{aligned} \mathcal{U}_{ij} = 2\pi\alpha_d \int \frac{d^2\mathbf{p}}{(2\pi)^2} \text{Tr} \left[G^A U^A G^A B_i G^R B_j \right. \\ \left. + G^A B_i G^R U^R G^R B_j \right], \end{aligned} \quad (3.51)$$

which has yet be dressed. The dressing amounts to replacing both B_i and B_j operators with the corresponding vertex corrected operators B_i^{vc} and B_j^{vc} , respectively.

The final result for the response of spin density is still given by Eq. (3.42), where the matrix $\mathcal{R} = \mathcal{F}(1 - \mathcal{F})^{-1}$ is, however, replaced with

$$\mathcal{R} = \frac{\mathcal{F}}{1 - \mathcal{F}} + \frac{1}{1 - \mathcal{F}} \mathcal{U} \frac{1}{1 - \mathcal{F}}, \quad (3.52)$$

which corresponds to diagrams Fig. 3.4c-d. It is again convenient to consider a particular basis for the matrix \mathcal{F} as defined in Eq. (3.41) to simplify analytical computation.

The problem of divergence in the operators \bar{B}_z does now become less trivial. Careful analysis shows that the linear terms in \mathbf{m} included in Eq. (3.52) lead to additional diverging contributions to δs^- of the form

$$\delta s_{\text{div},\alpha}^{-(1)} \propto -R_\infty n_\alpha \mathbf{m} \cdot \frac{\partial \mathbf{m}}{\partial t}, \quad (3.53)$$

that is analogous to the one in Eq. (3.47) for a finite m . (We remind that the constraint $n^2 + m^2 = 1$ provides a relation between these terms). The contribution

in Eq. (3.53) is, however, of too high order in \mathbf{m} in Eq. (3.5a) and cancels out completely in Eq. (3.5b).

The terms linear in \mathbf{m} are also responsible for diverging contributions in δs_α^+ of the type

$$\delta s_{\text{div},\alpha}^+ \propto R_\infty m_\alpha \mathbf{n} \cdot \frac{\partial \mathbf{n}}{\partial t} = -R_\infty m_\alpha \mathbf{m} \cdot \frac{\partial \mathbf{m}}{\partial t}, \quad (3.54)$$

that appear to be of higher than a linear order in \mathbf{m} , thus, exceeding our working precision.

Overall, one can show that the operators \bar{B}_ζ can be formally excluded by projecting the operator space of B_i operators on the corresponding subspace. The latter is facilitated by the transformation $\mathcal{F} \rightarrow P\mathcal{F}P$, where

$$P = 1 - \sum_{\zeta=0,z} \mathbf{a}_\zeta \mathbf{a}_\zeta^\dagger, \quad (3.55)$$

is the projection operator. Here, \mathbf{a} stands for the column vector and \mathbf{a}^\dagger for the corresponding conjugated string vector. Eq. (3.55) facilitates the regularized computation of the vertex corrections and lead to the results presented in the paper.

